Simulations of External Shocks in Gamma-Ray Bursts

Sarah Wellons

Advisor: Anatoly Spitkovsky

Submitted in partial fulfillment

of the requirements for the degree of

Bachelor of Arts

Department of Astrophysical Sciences

Princeton University

May 2011

I hereby declare that I am the sole author of this thesis.

I authorize Princeton University to lend this thesis to other institutions or individuals for the purpose of scholarly research.

Sarah Wellons

I further authorize Princeton University to reproduce this thesis by photocopying or by other means, in total or in part, at the request of other institutions or individuals for the purpose of scholarly research.

Sarah Wellons

Abstract

We present and discuss 2D simulations of relativistic collisionless shocks produced by a jet of plasma moving through a stationary medium, akin to the external shocks in gamma-ray bursts (GRBs) between the GRB jet and the interstellar medium (ISM). We examine properties of the shocks which would affect emission, including self-generated magnetic fields at the forward and reverse shocks, particle acceleration across the shock fronts, and mixing between the two plasmas at the contact discontinuity. From these simulations, we generate the radiation spectra that would be produced by synchrotron emission of the shocked particles and decompose this emission into its forward and reverse shock components. We find that a high density contrast between the two plasmas produces a more luminous spectrum, and that emission is dominated by particle acceleration at the reverse shock.

Acknowledgements

First and foremost, I would like to thank Anatoly Spitkovsky for his guidance throughout this project, and for the use of his valuable knowledge, time and resources. Thanks also to Luis Gargate, whose computational backup and knowledge of TRISTAN helped me out of many a tight spot, Dimitrios Giannios for helping me untangle the analytics of relativistic shock physics, and Lorenzo Sironi for the use of his radiation spectrum code. Finally, a special thanks to the juniors of Team Astro who filled Room 29 with laughter, camaraderie and leftover snacks, and to my family for all their love and support.

For my parents Helen and Michael Wellons, who taught me that kindness and integrity are greater virtues than intelligence.

Contents

List of Figures

Chapter 1

Introduction

1.1 Gamma-Ray Bursts

1.1.1 Description and Properties

The short, intense pulses of gamma-rays known as gamma-ray bursts (GRBs) are some of the most energetic phenomena in our universe. In a matter of seconds, they emit 10^{51} erg, roughly the amount of energy emitted by the Sun in its entire lifetime. They may vary in duration from a fraction of a second to several hundred seconds. Though there exist many possible progenitors for GRBs, including massive stars, mergers of compact objects, and magnetars, their exact origin is unknown. It is clear that GRB progenitors must be capable of producing a large amount of energy in a short amount of time.

Before the discovery that GRBs are "jetted," that is, that the emission is collimated rather than emitted isotropically, this energy release was believed to be even larger, on the order of 10^{52} to 10^{54} erg. On the higher end, that would be an energy release roughly equal to the rest mass energy of the Sun over merely seconds of emission! In addition to reducing the energy requirement for GRB progenitors, jetting is supported by the observation of achromatic breaks in the lightcurves of several GRBs,

produced as the jet is slowed by its movement through the interstellar medium (ISM) (Rosswog & Bruggen, 2003).

In order to emit gamma rays, the outflow from the GRB must also be relativistic. In the absence of relativistic expansion, the gamma rays would have high optical depth to pair production – all of the gamma rays would have interacted with photons to produce electron-positron pairs, and none would escape to be observed. The emission of gamma rays implies that the radiating material is expanding relativistically, lowering the optical depth to pair production and allowing the gamma rays to escape (Bloom, 2011).

Observationally, the signature of a GRB may be decomposed into two distinct eras: the prompt emission and the afterglow. The prompt emission contains the gamma rays from which the phenomenon draws its name, and the afterglow is a more long-lasting phenomenon visible in the x-ray, optical, and radio bands. The observational properties of this emission are most popularly explained by the fireball model.

1.1.2 The Fireball Model and External Shocks

The fireball model for GRBs explains their properties through a combination of internal and external shocks (Piran, 2004). External shocks, the subject of this thesis, occur between the relativistically moving GRB material and the stationary, much more diffuse ISM material. These shocks are highly relativistic, much more so than the internal shocks, and are believed to produce the GRB afterglow.

The prompt emission, on the other hand, is believed to originate from mildly relativistic internal shocks within a highly relativistic jet. These internal shocks are produced when the inner material of the jet, which is slightly faster, catches up with the external material that has been slowed by interactions with the ISM.

This combination of shock types is necessary to reproduce the observational prop-

erties. External shocks convert energy very efficiently, but are necessarily smooth and do not produce the observed variability. Internal shocks, on the other hand, satisfy the condition for variability but do not have the necessary efficiency of energy conversion. In this thesis, we simulate the external shock in a GRB between the outermost GRB material and the ISM, and explore its properties such as magnetic field generation, particle acceleration, and the degree of mixing in order to better understand the phenomena that produce such spectacular emission.

1.2 Motivation

1.2.1 Particle acceleration

One of the major components of nonthermal emission in astrophysical objects is particle acceleration. In shocks, particles may undergo Fermi acceleration when traveling across a shock front. Each time a particle crosses the shock front, it gains energy, and after bouncing back and forth several times can be accelerated to very high velocities. Previous simulations have demonstrated evidence of Fermi acceleration across a shock (Spitkovsky, 2008), and we now use the same method to examine the efficiency of acceleration in a multi-plasma interaction.

In the case of a GRB-ISM interaction, particles may experience Fermi accleration in two regions – the forward shock and the reverse shock – but it is unknown which shock front accelerates particles more efficiently and produces the majority of the nonthermal emission observed in GRBs. To explore this effect, we compare the acceleration produced at the forward and reverse shocks in our simulations. By varying the speed and density contrasts of the plasmas comprising the shocks, we may also better understand when Fermi acceleration is produced and how efficient we may expect it to be under many conditions.

1.2.2 Magnetic field production

The spectrum produced by a GRB afterglow is dependent on the magnetic fields present in the environment of the emitting material. Particles producing synchrotron radiation, for example, require the presence of a magnetic field for acceleration. We will examine and compare the magnetic fields produced in our simulations at the forward and reverse shocks, specifically questioning the following: How do the field strengths differ, both in peak magnitude and in width? How do they change with different density ratios between the GRB and ISM? How do they vary with the Lorentz factor of the jet?

1.2.3 Mixing at contact

The classical assumption that is made about shocks with more than one type of plasma is that they meet at a "contact discontinuity" between the forward and reverse shocks, and that each of the two plasmas is strictly restricted to one side of this boundary. In fact, however, there may be significant mixing between the two, which would affect the shape of the shock as well as the emitted spectrum. Additionally, a magnetic field may be generated at the contact, which would further affect emission as described in the previous section. To examine the effects of a non-sharp contact discontinuity, we decompose the shock into its jet and ISM components to determine the extent of mixing between the two plasmas and the conditions under which it occurs.

1.3 Outline

In Chapter 2, we discuss the shock structure and density compression within the shocked region, and derive analytically the expectations for the compression ratios in the limits of an ultrarelativistic reverse shock and a Newtonian reverse shock. In Chapter 3, we describe the methods of the simulation code TRISTAN-MP and the

setup of our particular problems. In Section 4.1, we present simulations of shocks formed using a single plasma, and in Section 4.2, we present simulations of two-plasma shocks and examine their properties as described in Section 1.2. In Chapter 5 we present and discuss the radiation spectra that would be generated by the simulated shocks. Finally, in Chapter 6 we discuss the results, and conclude.

Chapter 2

Shock Structure

For an external GRB shock, the consituent charged particles have a long mean free path between Coulomb collisions, so we consider the shocks to be collisionless. That is, the particles that comprise the shock do not interact through individual Coulomb collisions, but rather through the production of collective electromagnetic fields. In this section, we consider analytically the interaction of two plasmas across the boundary of a shock front, and derive the expected density ratios of the shocked regions. In Chapter 4 and onward, we use values calculated using this analytical method in comparison with the results of the shock simulations, to see whether the code returns the expected results, and under what circumstances.

2.1 Compression ratio across a shock

To determine the mass density ratio across a relativistically moving shock, we follow a derivation similar to that performed by Johnson & McKee (1971), but for a general adiabatic index Γ. In the extreme relativistic limit, the pressure of a fluid is

$$p = (\Gamma - 1)E \equiv \alpha E,$$

where E is the energy density. When the rest energy is non-negligible,

$$p = \alpha(E - nmc^2), \tag{2.1}$$

where n is the proper nucleon density, m is the mass of the nucleon, and c is the speed of light.

In the frame of the shocked fluid, we define $c\beta$ to be the velocity of the unshocked fluid with $\gamma = (1-\beta)^{-1/2}$, and $c\beta_s$ to be the velocity of the shock front itself. Then the continuity equations across the shock are

$$\begin{aligned} p &= \gamma^2 n_0 mc^2(\beta + \beta_s)\beta, & (2.2)\\ E\beta_s c &= \gamma^2 n_0 mc^2(\beta + \beta_s)c, & (2.3)\\ n\beta_s c &= \gamma n_0(\beta + \beta_s)c. & (2.4) \end{aligned}$$

where n and n_0 are the proper nucleon densities of the shocked and unshocked fluids respectively. Combining Eqns. 2.3 and 2.4,

$$E/nmc^2 \equiv \mu = \gamma, \tag{2.5}$$

where μ is defined to be the ratio of the proper energy to the nucleon rest energy. To find the shock velocity, we note that from Eqns. 2.2 and 2.3,

$$\beta_s = \frac{p}{E\beta},$$

where

$$\beta = \sqrt{\frac{\gamma^2 - 1}{\gamma^2}} = \sqrt{\frac{(\mu-1)(\mu+1)}{\mu^2}}$$

and from Eqns. 2.1 and 2.5,

$$\frac{p}{E} = \alpha\left(1 - \frac{nmc^2}{E}\right) = \alpha\left(1 - \frac{1}{\gamma}\right) = \alpha\frac{\mu - 1}{\mu}.$$

Combining these, the shock velocity is

$$\beta_s = \alpha\sqrt{\frac{\mu - 1}{\mu + 1}}. \tag{2.6}$$

Finally, to calculate the compression ratio we see that from Eqn. 2.4,

$$\begin{aligned}
\frac{n}{n_0} &= \frac{\gamma(\beta + \beta_s)}{\beta_s} = \mu\left(1 + \frac{\beta}{\beta_s}\right) \\
&= \mu\left(1 + \sqrt{\frac{\mu^2 - 1}{\mu^2}}\left(\alpha\sqrt{\frac{\mu - 1}{\mu + 1}}\right)^{-1}\right) \\
&= \mu\left(1 + \frac{\mu + 1}{\alpha\mu}\right) \\
&= \frac{1}{\alpha} + \left(1 + \frac{1}{\alpha}\right)\mu \\
\frac{n}{n_0} &= \frac{1 + \Gamma\mu}{\Gamma - 1},
\end{aligned} \tag{2.7}$$

where we have also invoked Eqns. 2.5 and 2.6. For an adiabatic index $\Gamma = 4/3$, this simplifies to $4\mu + 3$ and we recover the result from Johnson & McKee (1971). In our case, we will be taking the adiabatic index to be $\Gamma = 3/2$, so that

$$\frac{n}{n_0} = 3\mu + 2. \tag{2.8}$$

2.2 Two-plasma shocks

In the context of a gamma-ray burst shock, there are four regions of interest: (1) the unshocked ISM, (2) the shocked ISM, (3) the shocked GRB material and (4) the unshocked GRB material. Here the forward shock separates regions 1 and 2, a contact

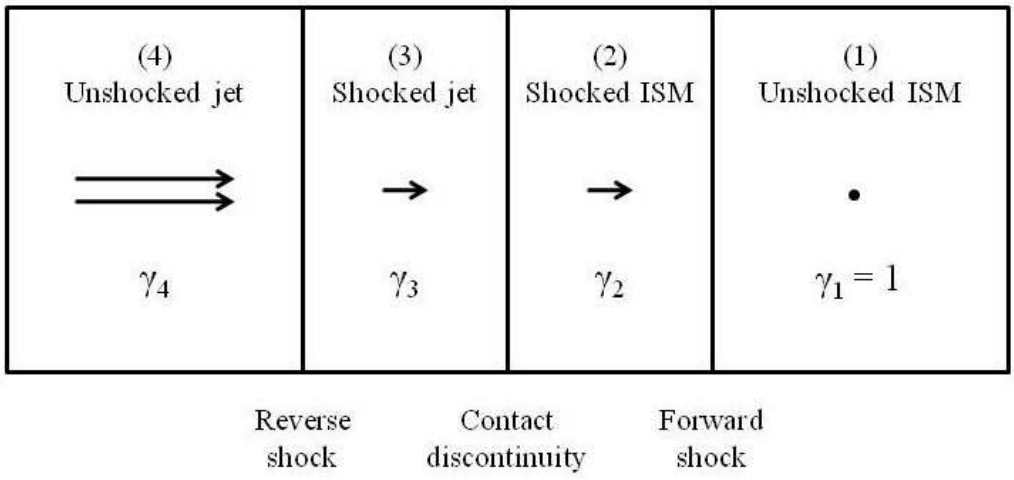

Figure 2.1: Shock structure

discontinuity separates regions 2 and 3, and the reverse shock separates regions 3 and 4 as depicted in Figure 2.1. Using the result from Section 2.1, the compression ratios for the forward and reverse shocks should be

$$\frac{n_2}{n_1} = 3\gamma_2 + 2 \tag{2.9}$$

$$\frac{n_3}{n_4} = 3\bar{\gamma}_3 + 2 \tag{2.10}$$

where n_x is the proper density of region x, γ_x is the Lorentz factor of region x with respect to region 1, and $\bar{\gamma}_3$ is the Lorentz factor of region 3 with respect to region 4.

Sari & Piran (1995) derive expressions for γ_2 and $\bar{\gamma}_3$ in the ultrarelativistic and Newtonian limits for the reverse shock. (The forward shock will always be ultrarelativistic when $\gamma_4 \gg 1$ and $n_4/n_1 \equiv f > 1/\gamma_4^2$, as is the case in all our simulations.) In the limit where the reverse shock is ultrarelativistic ($\gamma_4^2 \gg f$, $\bar{\gamma}_3 \gg 1$),

$$\bar{\gamma}_3 = \frac{\gamma_4^{1/2}}{\sqrt{2} f^{1/4}} \tag{2.11}$$

$$\gamma_2 = \gamma_3 = \frac{\gamma_4^{1/2} f^{1/4}}{\sqrt{2}} \tag{2.12}$$

and in the limit where it is Newtonian ($f \gg \gamma_4^2$, $\bar{\gamma}_3 - 1 \ll 1$),

$$\bar{\gamma}_3 = 2\epsilon + 1 \tag{2.13}$$

$$\gamma_2 = \gamma_3 = \gamma_4(1 - \sqrt{\epsilon}), \tag{2.14}$$

where

$$\epsilon = \frac{2\gamma_4^2}{7f}. \tag{2.15}$$

In our simulation setup, we are able to set the values of γ_4 and $\bar{f} = \bar{n_4}/\bar{n_1}$, the density ratio between the unshocked GRB material and ISM in the frame of the unshocked ISM. Because we are simulating everything in this frame, we would like to change all the expressions describing the shock to be in terms of $\bar{n_x} = \gamma_x n_x$, the density of region x with respect to the unshocked ISM. Thus we modify Eqns. 2.9 and 2.10 to become

$$\frac{\bar{n}_2}{\bar{n}_1} = \gamma_2(3\gamma_2 + 2) \tag{2.16}$$

$$\frac{\bar{n}_3}{\bar{n}_4} = \frac{\gamma_3}{\gamma_4}(3\bar{\gamma}_3 + 2) \tag{2.17}$$

where in the ultrarelativistic limit,

$$\bar{\gamma}_3 = \frac{\gamma_4^{3/4}}{\sqrt{2}\bar{f}^{1/4}} \tag{2.18}$$

$$\gamma_3 = \gamma_2 = \frac{\gamma_4^{1/4}\bar{f}^{1/4}}{\sqrt{2}}, \tag{2.19}$$

and in the Newtonian limit Eqns. 2.13 and 2.14 remain the same but

$$\epsilon = \frac{2\gamma_4^3}{7\bar{f}}. \tag{2.20}$$

Equations 1.13-14 and 1.16-20 form the basis of our expectations for the densities in the four regions formed in the simulations. For example, in a setting with an ultrarelativistic reverse shock where $\gamma_4 = 15$ and $\bar{f} = 4$, we expect that

$$\begin{aligned} \bar{\gamma}_3 &= \frac{(15)^{3/4}}{\sqrt{2}(4)^{1/4}} = 3.81 \\ \gamma_3 = \gamma_2 &= \frac{(15)^{1/4}(4)^{1/4}}{\sqrt{2}} = 1.97 \end{aligned}$$

so that

$$\begin{aligned} \frac{\bar{n}_2}{\bar{n}_1} &= 1.97(3(1.97) + 2) = 15.58 \\ \frac{\bar{n}_3}{\bar{n}_4} &= \frac{1.97}{15}(3(3.81) + 2) = 1.76. \end{aligned}$$

So, if the unshocked ISM were initialized with a density of 10 particles per cell (ppc), we would expect the shocked ISM to have a density of 155.8 ppc, the unshocked GRB material to have a density of 40 ppc, and the shocked GRB material to have a density of 70.4 ppc.

Similarly, in the case of a Newtonian reverse shock where $\gamma_4 = 4$ and $\bar{f} = 1000$, we expect that

$$\begin{aligned} \epsilon &= \frac{2(4)^3}{7(1000)} = 0.018 \\ \bar{\gamma}_3 &= 2(0.018) + 1 = 1.036 \\ \gamma_2 = \gamma_3 &= 4(1 - \sqrt{0.018}) = 3.46 \end{aligned}$$

so that

$$\begin{aligned} \frac{\bar{n}_2}{\bar{n}_1} &= 3.46(3(3.46) + 2) = 42.83 \\ \frac{\bar{n}_3}{\bar{n}_4} &= \frac{3.46}{4}(3(1.036) + 2) = 4.42. \end{aligned}$$

Then if the unshocked ISM again had a density of 10 ppc, we would expect to see shock structure form where the shocked ISM had a density of 428.3 ppc, the unshocked GRB material had a density of 1000 ppc, and the shocked GRB material had a density of 4420 ppc.

Chapter 3

Methods

3.1 TRISTAN

All of the simulations shown in this paper were run in 2D using TRISTAN-MP, a massively parallelized version of an electromagnetic code which uses the particle-in-cell (PIC) method (Buneman, 1993; Spitkovsky, 2005). Using this method, a plasma such as our GRB jet is represented as a collection of macroparticles. These particles are moved by integration of the relativistic equations of motion in accordance with their charge and mass. Their movement is recorded as current and deposited on a grid, which allows for the discretization of Maxwell's laws and the evolution of electromagnetic fields. These fields in turn determine the acceleration of the particles at the next timestep. Interpolation over sub-grid distances is performed linearly.

3.2 Setup of problems

The simulations are performed in an environment with a fixed length in the transverse direction (y) and periodic boundary conditions on the top and bottom. The horizontal length (x), by contrast, is not fixed, but rather increases as necessary throughout the simulation as the region of interest expands. The simulation box is initialized with

some amount of plasma, and as the box expands, more particles are injected on the left or right to maintain a continuous flow.

Resolution in time and space is determined by the plasma oscillation frequency

$$\omega_p = \sqrt{\frac{4\pi n e^2}{\gamma m}} \tag{3.1}$$

where n is the number density of the particles, e is the charge per particle, γ is the bulk Lorentz factor of the plasma, and m is the mass per particle. Both ω_p and the plasma skindepth c/ω_p must be resolved for the simulation to be stable. We typically set $c/\omega_p = 10$ cells for the medium upstream of the shock, with the exception of the highest density ratio cases in Section 4.2 where $c/\omega_p = 20$ cells (50:1 and 100:1) or $c/\omega_p = 30$ cells (200:1).

At the time of its injection, each particle is initialized with a certain mass and charge. To conserve computational resources, in situations where plasmas are being injected with different densities (as is the case for the ISM and GRB jet), we kept the number of particles per cell constant across the plasmas. Rather than injecting more particles to create a denser plasma, we injected the same number of particles but with more weight. For example, for a shock with a density ratio of 4 between the ISM and GRB, we might inject 10 particles per cell each with weight 1 for the ISM, but inject 10 particles per cell with weight 4 for the GRB. By injecting 10 heavy particles rather than 40 light ones, we experience a significant speed-up because we are tracking fewer particles. By its nature, this method of "clumping" particles together introduces more noise into the system, but comparisons of simulations performed at a 25:1 density ratio (as discussed later in Section 4.2) with various levels of particle weighting revealed little difference in the results. Here the benefit of particle weighting, a factor of roughly n speed-up for an n:1 density ratio, far outweighs its cost in noise.

Chapter 4

Simulation Results

4.1 Test Cases

Before trying a case analogous to a GRB-ISM shock, which requires two different plasmas, we performed several test cases which produce a shock with only one plasma.

4.1.1 Bouncing plasma off a wall

The simplest way to produce a single-plasma shock is to collide a moving plasma against a wall. Initially, this results in a density jump by a factor of two as the particles are reflected away from the wall. When the reflected and incoming particles interact with one another, an instability forms which slows both beams and creates a shock. The particles behind the shock are further compressed, and the plasma comes to rest. As more particles hurtle toward the wall, the compressed region increases in length away from the wall and the shock moves forward into the incoming beam of particles.

To set up this scenario, the simulation box is initialized to contain plasma moving at some Lorentz factor γ to the left. As the simulation progresses, an injector to the right of the plasma moves further to the right. At each timestep, a void is left

between the injector and the right edge of the plasma, produced jointly by the motion of the injector to the right and the motion of the plasma to the left, and the injector fills this space with plasma. We set the injector to move with the speed of light to outrun any electromagnetic fields that might be produced at the shock, so that the particles which are injected could not have had any interaction with the shock at the time of their injection.

On the left side, at each timestep all particles which lie to the left of the wall are identified by their x-position. Their x-velocities are then reversed as if they had bounced off the wall at that point. These particles form the beam of reflected particles whose interaction with the incoming particles produce the shock front.

One such shock, where the plasma approaches the wall with a Lorentz factor $\gamma = 5$ is shown in Figure 4.1, and another where the plasma has Lorentz factor $\gamma = 2$ is shown in Figure 4.2.

On the right side of each figure, the incoming plasma rushes in with a density $n = 10$ particles per cell (ppc). When it hits the shock, the plasma is compressed to a density $n \approx 31$ ppc for $\gamma = 5$ and $n \approx 33$ ppc for $\gamma = 2$ on the left.

From Section 2.1, we expect that

$$\frac{n_2}{n_1} = 3\bar{\gamma}_{1,2} + 2$$

where n is proper density, the subscript 1 refers to the unshocked region and 2 refers to the shocked region, and $\bar{\gamma}_{1,2}$ is the Lorentz factor between the two regions. Expressing this in terms of $\bar{n}$, the densities in the frame of the wall (our frame), we find that

$$\frac{\bar{n}_2}{\bar{n}_1} = \frac{\gamma_2}{\gamma_1}(3\bar{\gamma}_{1,2} + 2). \tag{4.1}$$

If we assume that the wall completely stops the shocked material and take $\gamma_2 \approx 1$

and $\bar{\gamma}_{1,2} \approx \gamma_1$, this simplifies to

$$\frac{\bar{n}_2}{\bar{n}_1} = 3 + \frac{2}{\gamma_1}, \tag{4.2}$$

so we expect that the density ratio between the two regions should be approximately 3, and should approach 3 for higher γ. This coincides with our simulated density ratios of 3.1 for $\gamma = 5$ and 3.3 for $\gamma = 2$.

Looking at the 2D structure of the shocks in Figures 4.1 and 4.2, filamentation ahead of the shock is visible both in density and magnetic field. These filaments are more pronounced as well as more numerous in the case where $\gamma = 2$, and less well-formed in the case where $\gamma = 5$.

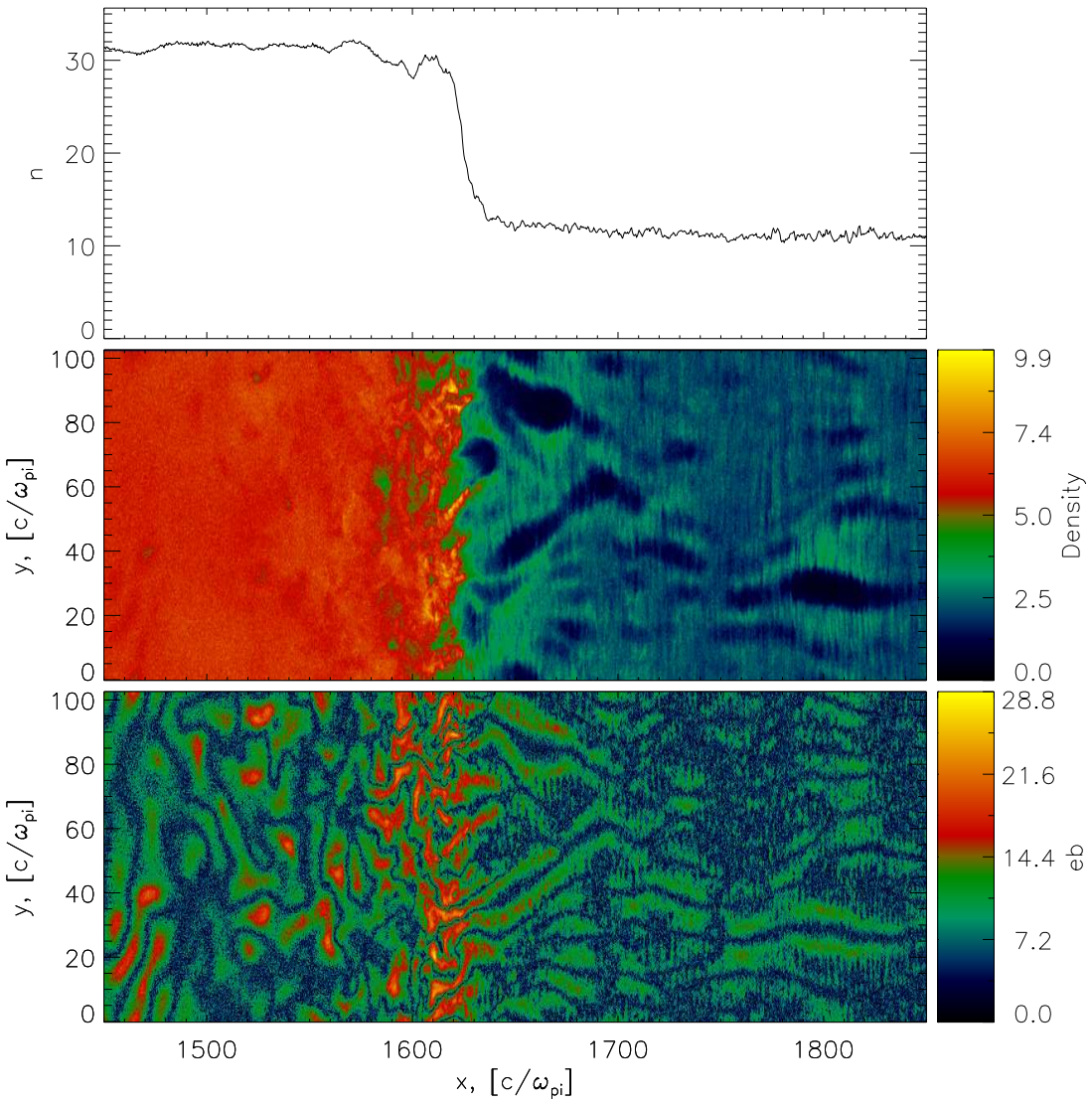

Figure 4.1: Shock formed by colliding a stream of plasma at $\gamma = 5$ into a stationary wall at $\omega_p t = 3644$. (Note: the numbers on the color bar have been scaled for contrast.) Top panel: density summed over the y-direction. Middle panel: 2D density. Bottom panel: 2D magnetic field energy.

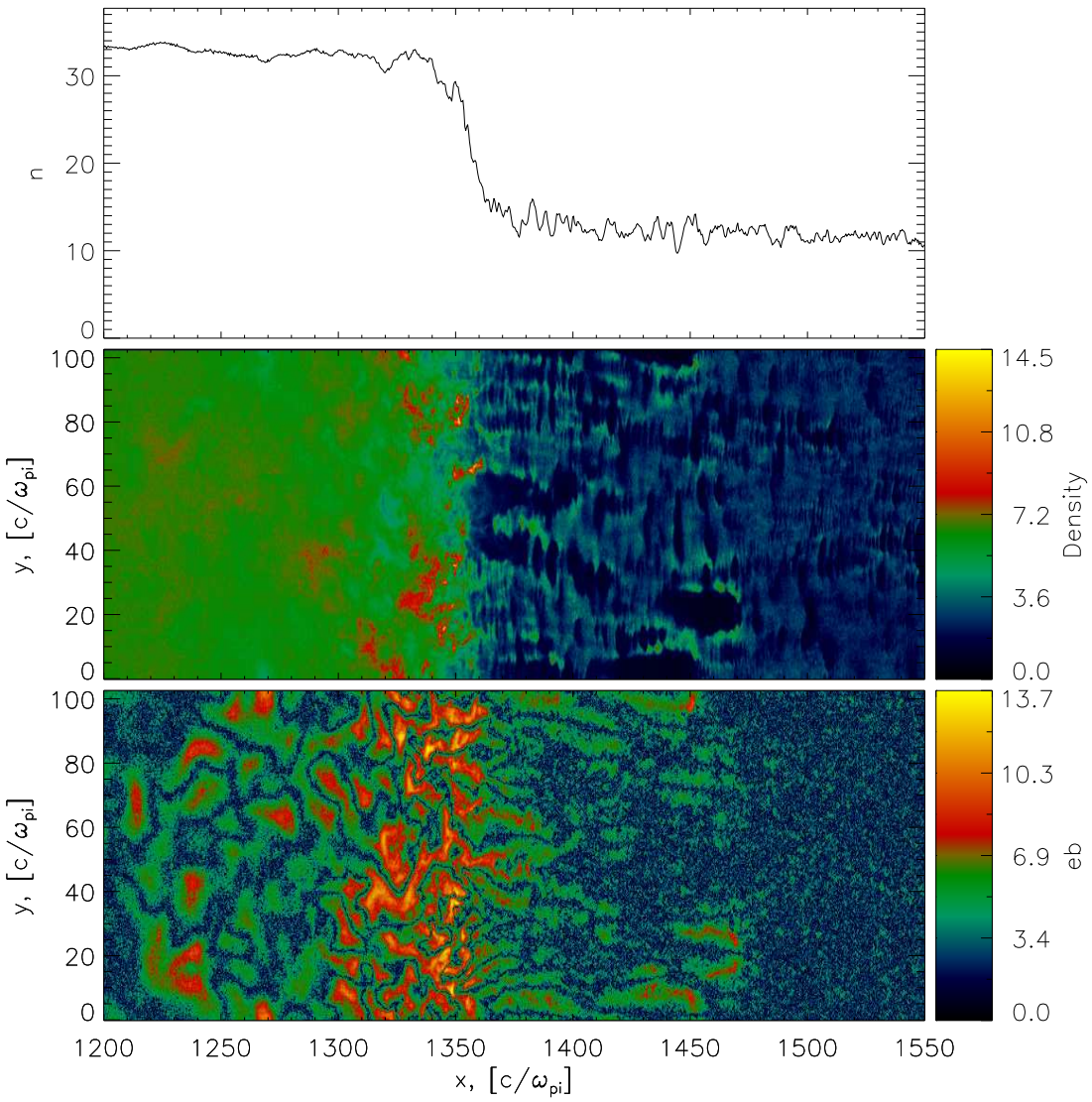

Figure 4.2: Shock formed by colliding a stream of plasma at $\gamma = 2$ into a stationary wall at $\omega_p t = 3712$. Top panel: density summed over the y-direction. Middle panel: 2D density. Bottom panel: 2D magnetic field energy.

4.1.2 Pushing plasma with a piston

An equivalent scenario to that from Section 4.1.1, except in a different frame of reference, is to have the wall approaching the plasma rather than the plasma approaching the wall. From a computational standpoint, this is an improvement on the previous case because the plasma is at rest. Moving plasma, such as that in the previous section, is susceptible to instabilities. When we switch to the frame of the unshocked plasma, the plasma does not have to travel from the injector before hitting the shock, but rather it waits for the shock to come to it. In this case, we initialize the box to contain stationary plasma (and inject more on the right as the simulation proceeds), and move the wall with Lorentz factor γ through the plasma. The wall pushes the plasma as it moves forward, acting as a piston, and a shock forms between the pushed and stationary plasma.

In this case, because we are no longer in the frame of the wall, we can no longer apply a simple reflection of the particle's x-velocity. Now, any particle which is pushed by the wall also receives a "boost" from the wall's relativistic motion. Thus the x-component of its relativistic 4-velocity, $u_x = \gamma\beta_x$, becomes

$$u'_x = \gamma_w^2\gamma(2\beta_w - \beta_x(1+\beta_w^2)), \tag{4.3}$$

where the subscript w denotes the wall. (See Appendix A for a derivation.) This boost is applied to any particle which is found behind the current position of the wall at a given timestep and is moving with $\beta < \beta_w$.

Figures 4.3 and 4.4 show the analogs to Figures 4.1 and 4.2 respectively for this case. In Figure 4.3, the shock is formed by a piston moving with $\gamma = 5$, and in Figure 4.4, it is formed by a piston moving with $\gamma = 2$.

The plasma on the right side of each figure is stationary with Lorentz factor $\gamma = 1$. The shock wave in the middle is formed by the incoming plasma that has been

compressed by the piston on the right side. As in the previous section, the plasma on the right starts off with an initial density of 10 ppc. (Some figures may appear to have a higher density on the right, but they are zoomed in to focus on the shock and would settle down to 10 ppc if the figure were extended.) In the case where the piston moves with $\gamma = 5$, the shocked plasma is compressed to $n \approx 770$ ppc, and at $\gamma = 2$ it is compressed to $n \approx 130$ ppc.

From the previous section, we still expect that

$$\frac{\bar{n}_2}{\bar{n}_1} = \frac{\gamma_2}{\gamma_1}(3\bar{\gamma}_{1,2} + 2).$$

In this case, however, the plasma on the right has Lorentz factor $\gamma_1 = 1$ and thus $\bar{\gamma}_{1,2} = \gamma_2 \approx \gamma_{piston}$. Applying these assumptions, we find

$$\frac{\bar{n}_2}{\bar{n}_1} = \gamma_2(3\gamma_2 + 2). \tag{4.4}$$

Comparing the scenarios from this section and the previous section 4.1.1 with the same γ (that is, γ_1 of the moving plasma from Sec. 4.1.1 is the same as γ_2 of the piston from this section), the compression ratios can be summarized as

$$\left(\frac{\bar{n}_2}{\bar{n}_1}\right)_{wall} = 3 + \frac{2}{\gamma} \tag{4.5}$$

$$\left(\frac{\bar{n}_2}{\bar{n}_1}\right)_{piston} = \gamma(3\gamma + 2), \tag{4.6}$$

or, combining the two,

$$\left(\frac{\bar{n}_2}{\bar{n}_1}\right)_{piston} = \gamma^2 \left(\frac{\bar{n}_2}{\bar{n}_1}\right)_{wall}. \tag{4.7}$$

Our simulated shocks match these analytical results. For the case where $\gamma = 2$, the compression ratio in the wall frame previous section was 3.3, so we expect that in the plasma frame it should be $3.3 \times 4 = 13.2$, which matches our result of ≈ 13. Similarly,

for $\gamma = 5$, we expect to have a compression ratio of $3.1 \times 25 = 77.5$, which matches our result of ≈ 77.

Because these simulations progressed to a later $\omega_p t$, the filaments ahead of the shock are more well-formed in Figures 4.3 and 4.4 in the piston case than they had been in Figures 4.1 and 4.2 in the stationary wall case. In Figure 4.3, for example, six clearly defined density filaments have formed in front of the $\gamma = 5$ shock over a y-distance 50 c/ω_p. Roughly the same number of filaments form in the $\gamma = 2$ case, though their structure is less distinct.

The magnetic field structure produced in the piston case also differs from the stationary wall case. In the previous section, the medium downstream of the shock had been at rest, but we have now shifted to a frame where the downstream medium moves at $\gamma = 5$ or $\gamma = 2$. This results in the field structure appearing contracted at higher γ. Features which appeared roughly circular in Figures 4.1 or 4.2 now appear elliptical and elongated in the y-direction in Figures 4.3 and 4.4, with higher eccentricity for higher γ.

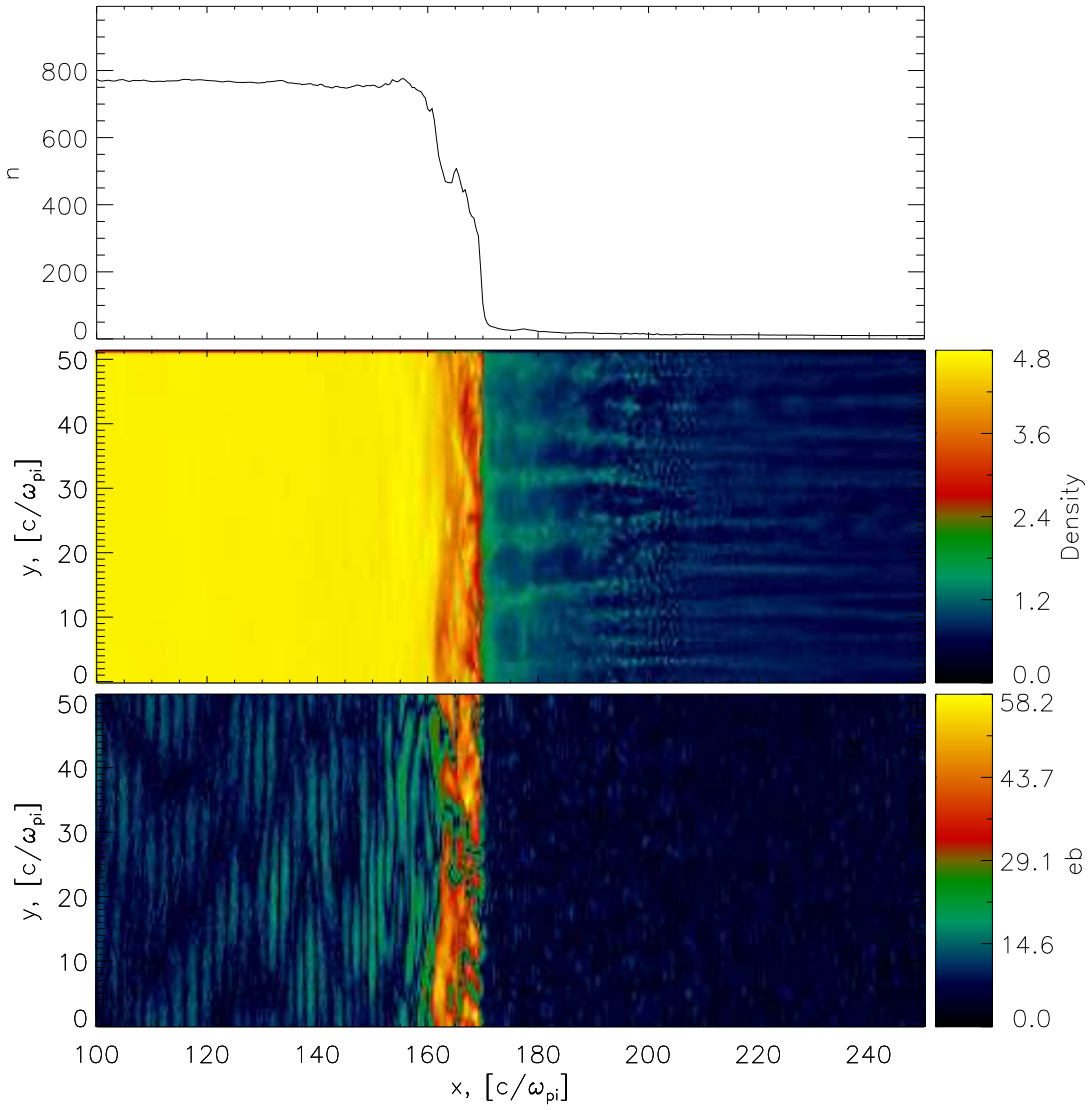

Figure 4.3: Shock formed by moving a piston at $\gamma = 5$ into stationary plasma at $\omega_p t = 9585$. Top panel: density summed over the y-direction. Middle panel: 2D density. Bottom panel: 2D magnetic field energy.

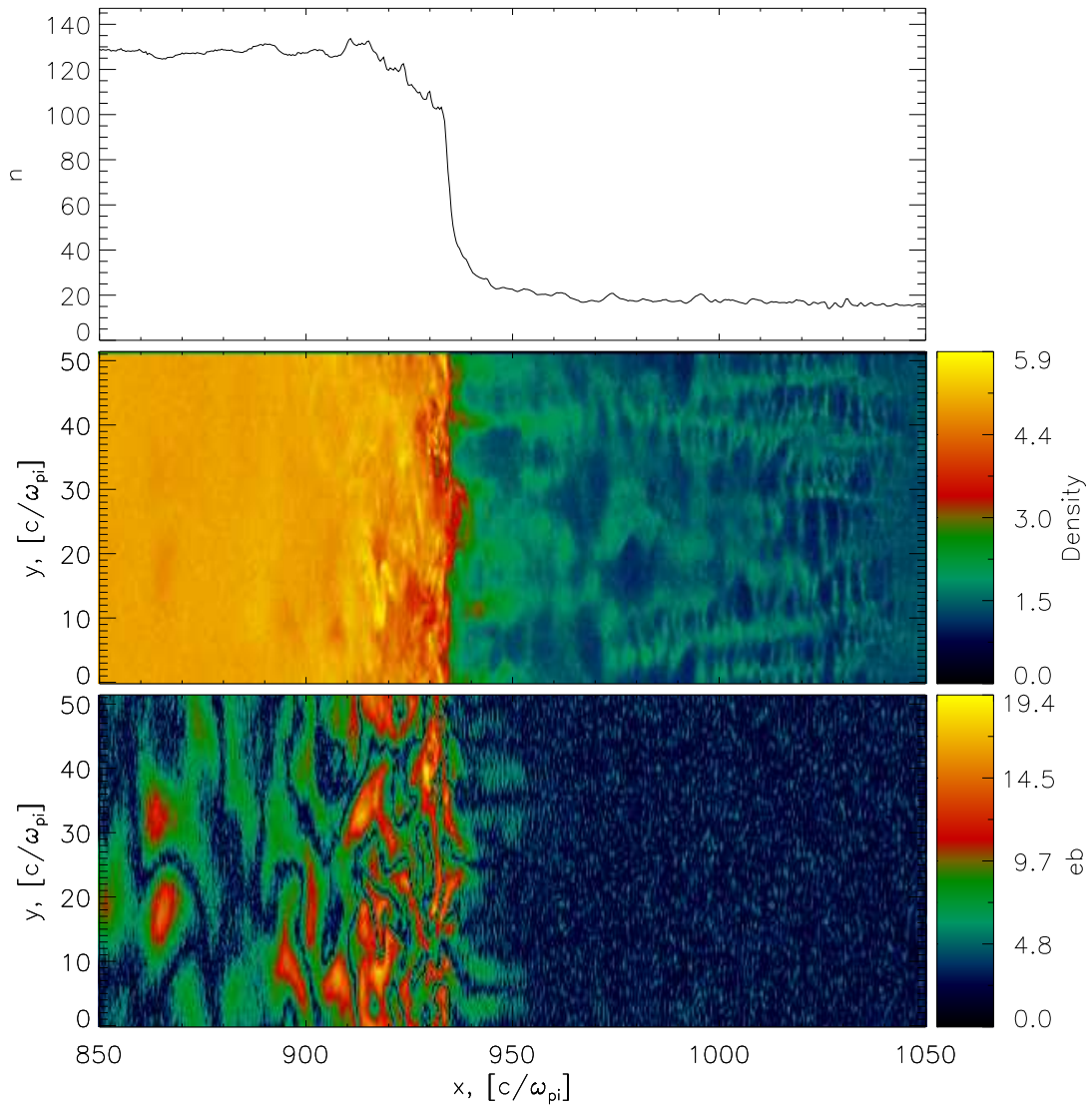

Figure 4.4: Shock formed by moving a piston at $\gamma = 2$ into stationary plasma at $\omega_p t = 12644$. Top panel: density summed over the y-direction. Middle panel: 2D density. Bottom panel: 2D magnetic field energy.

4.2 Colliding Jets

In the final scenario, we introduce a second type of plasma: the GRB jet. Previously, we had injected slow or stationary plasma on the right, and used a wall to produce a shock. In this case, we populate the box with stationary plasma on the right, representing the ISM, and inject relativistically-moving plasma on the left, representing the GRB jet. When the GRB material collides with the ISM, the four regions shown in Figure 2.1 are formed: the unshocked GRB, the shocked GRB, the shocked ISM, and the unshocked ISM, where the regions are separated by the reverse shock, contact discontinuity, and forward shock respectively (although, as we shall see, these boundaries are not as impenetrable as they may seem).

To reduce the instability experienced by moving plasma, we implemented a moving injector on the left which follows behind the reverse shock. This serves the dual purposes of keeping the jet particles from traveling too far before interacting with the shock, as well as reducing the total number of particles that have been injected, affording both a speed-up as well as increased stability.

Figure 4.5 shows the shock formed by a jet at $\gamma = 15$ colliding with stationary plasma ten times less dense. As in the figures from Section 4.1, the top panel depicts the 1-dimensional density along the x-axis, the middle panel 2-dimensional density along the x- and y-axes, and the bottom panel the 2-dimensional magnetic field energy. The jet on the left has a density of 40 ppc and encounters the stationary plasma on the right with a density of 4 ppc. The forward shock is visible both as a jump in density and in magnetic field around x = 1400, and the material in the forward shock region is compressed to more than 80 ppc at the peak. The reverse shock is also accompanied by a jump in density and magnetic field around x = 1200, and reaches a density of roughly 60 ppc.

The filaments ahead of the forward shock exhibit the same sort of structure and density observed in the piston case from Section 4.1.2. There are 12 clearly defined

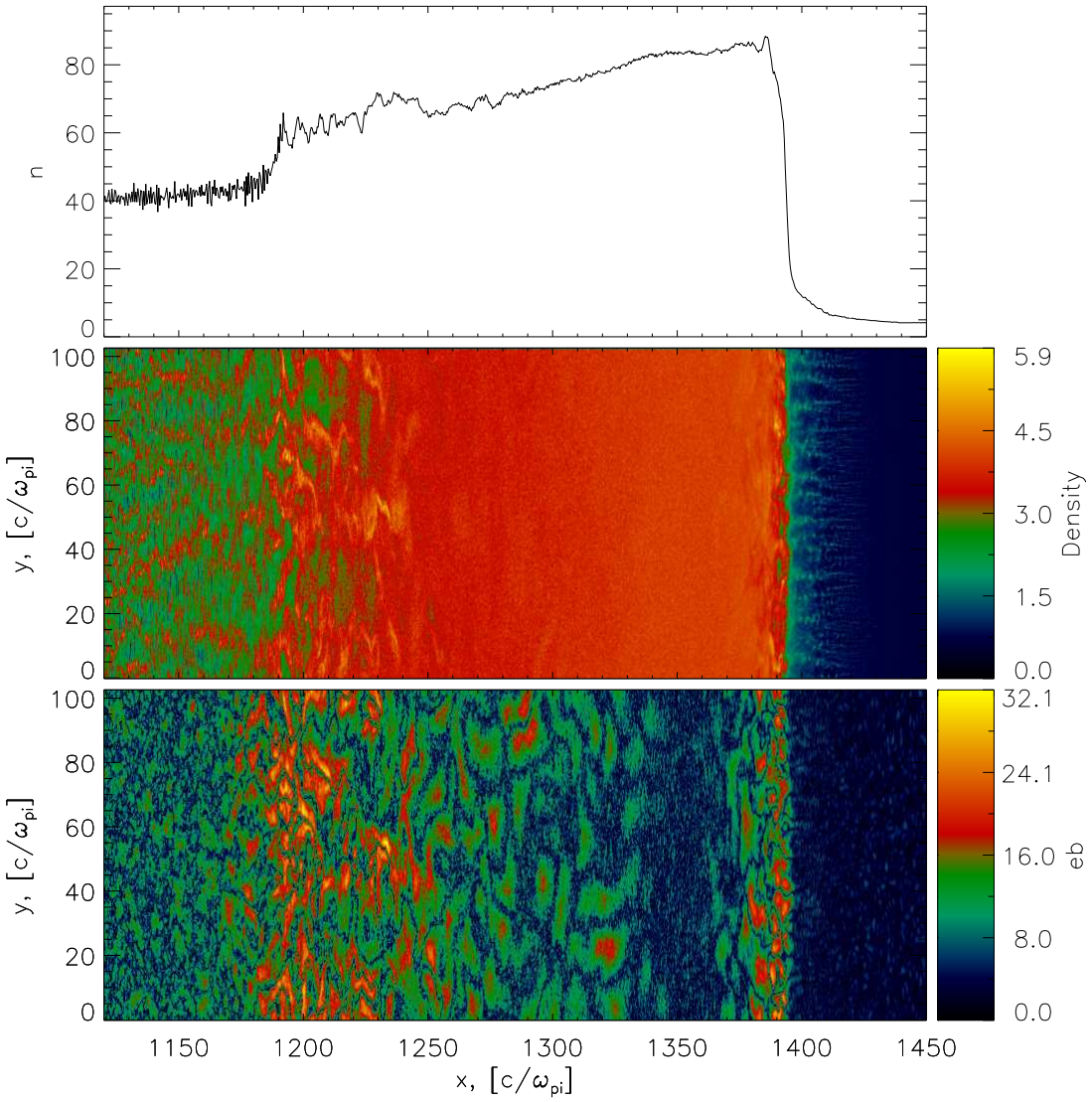

Figure 4.5: Shock formed by colliding a jet moving at $\gamma = 15$ into stationary plasma ten times less dense at $\omega_p t = 1439$. Top panel: density summed over the y-direction. Middle panel: 2D density. Bottom panel: 2D magnetic field energy.

filaments visible reaching ahead of the shock over a distance $c/\omega_p = 100$, the same density as in Figure 4.3. The magnetic field structure at the forward shock is also analogous to the piston case, with structure similar to that in Figure 4.4. Though the level of compression and the relative strengths of the magnetic fields vary, this same basic structure forms in all of the simulations described in this section.

All the following simulations were performed with a jet having Lorentz factor $\gamma = 15$, but with different density ratios between the jet and ISM plasmas. We compare the compression ratios, level of mixing, particle acceleration efficiency, and magnetic field strength across these different density ratios.

4.2.1 Compression and Mixing

Figure 4.6 at the end of this subsection depicts the evolution in the density profile of a shock formed with a jet and ISM of equal density. The "contact," which in this case is defined to be the place where the two plasmas have the same density, is fixed at x = 0, and as the simulation progresses (from the yellow lines to the black lines), the forward shock moves to the right, the reverse shock moves to the left, and the shocked region grows. The top panel shows the density profile evolution for both plasmas together, and the bottom two panels separate it into its two components, the jet and the ISM. The orange lines on each panel indicate the predictions for density from Chapter 2 in the case of an ultrarelativistic reverse shock, where the solid line is the prediction for the forward shock and the dotted line is the prediction for the reverse shock.

Following that, Figure 4.7 shows the profile of $\gamma_x < \beta_x >$ at a given x-position in the top panel, where $\gamma_x = (1 - < \beta_x >^2)^{-1/2}$. The bottom two panels show the phase space for the jet and ISM components separately. The subsequent Figures 4.8 to 4.19 show the density profile, velocity profile, and phase space for shocks formed with density ratios of 4:1, 10:1, 25:1, 50:1, 100:1, and 200:1 respectively.

For the 1:1 shock shown in Figure 4.6, it is clear that the expectations for the compression ratios in the forward and reverse shocks are met. The forward shock develops the expected compression ratio of ≈ 8.5 by $\omega_p t = 1800$, and does not evolve beyond that except to expand. The reverse shock here is less dramatic than the forward shock, reaching the expected compression of only ≈ 1.6 by $\omega_p t = 1125$, and also remains at its expected value as the shock evolves. (The drop down to 0 on the left is not a physical feature, but the location of the left injector.) Although the regions in the direct vicinity of the shock fronts behave as expected in terms of density, the intermediate region experiences a significant amount of unexpected mixing. After reaching its peak compression at the forward shock, the density falls slowly toward the contact, rather than remaining constant and dropping suddenly as we would expect in a strictly segregated system. The reverse shock, conversely, maintains a constant density until the contact, and then slowly decreases. Surprisingly, a significant amount of jet material penetrates all the way through the shock into the region ahead of the forward shock. These jet particles are also visible in the phase space in Figure 4.7. At low density ratios (including, of course, 1:1), the forward shock moves more slowly because there is less material pushing it. Consequently, it is easier for the jet particles moving at $\gamma = 15$ to outrun the slow forward shock.

At the other extreme of density contrasts, Figure 4.18 shows the evolution in density of a shock formed with a jet 200 times denser than the ISM. The reverse shock, despite remaining at a steady value, fails to reach the predicted compression at the very top of the plot. Interestingly, the ISM component of the forward shock alone does not manage to reach the density prediction for the forward shock, but when combined with the jet material which manages to penetrate that far, the shocked region does reach the predicted value. Similar to the previous case, there is a gradual lessening in density between the two shocks, rather than two distinct regions of shocked material. In this case, however, it is not the jet material which penetrates through the forward

shock, but the ISM material which penetrates through the reverse shock. These same ISM particles are visible in the ISM phase space depicted in Figure 4.19.

At the intermediate density ratios, the shocks exhibit characteristics between these more extreme examples. As a general trend, the higher the density ratio, the less agreement between the analytical expectation for compression ratios and the density of the simulated shocks. This is unsurprising because at higher density ratios the reverse shocks are slower, and don't fit the requirements for being "ultrarelativistic" as well as for lower density ratios. Although there is mixing between the two plasmas at all density ratios, at low density ratios there is more penetration of the jet into the forward shock, and at high density ratios there is more penetration of the ISM into the reverse shock. In general, it also seems that the reverse shock forms and reaches a steady state fairly quickly, while the forward shock may take longer. In most of the cases plotted, the reverse shock reaches its final density by the first or second time plotted but the forward shock does not fully form until the third or fourth. This is especially true at high density ratios, where the forward shock must accrue a very high level of compression.

In the test cases of the stationary wall and piston, the shock produced a sharp jump in density, evenly separating the regions of shocked and unshocked plasma. Furthermore, the shocked region maintained a constant density. The shocks generated in these two-plasma simulations do not exhibit this behavior – the density jump at the forward shock may not be very steep, especially at high density ratios, and the density profiles are universally not flat in the shocked regions. These differences may be attributed to the allowance of mixing between the two types of plasma. Rather than being reflected at the contact as assumed in the wall and piston cases, particles from the ISM may creep into the jet, and vice-versa. This lack of a sharp contact allows the density profile to become non-constant in the shocked region and the forward shock to become less steep.

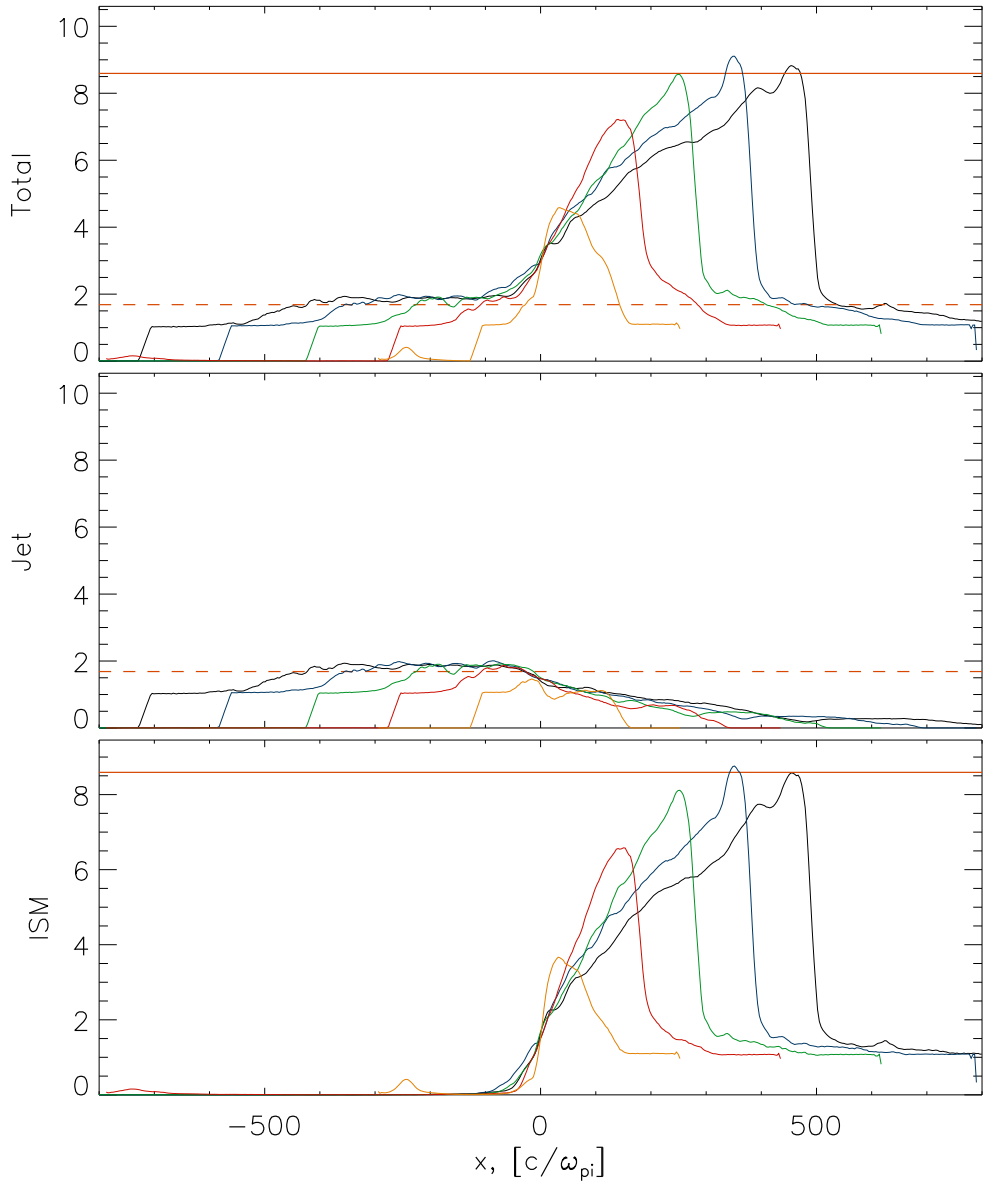

Figure 4.6: The evolution in density of a shock formed by a jet at $\gamma = 15$ colliding with a stationary plasma at the same density, at $\omega_p t = 450$, 1125, 1800, 2475, and 3149. The orange lines indicate the predictions for density in the case of an ultrarelativistic reverse shock, where the prediction for the forward shock is solid and the prediction for the reverse shock is dashed. Top panel: Combined density. Middle panel: Jet density only. Bottom panel: ISM density only.

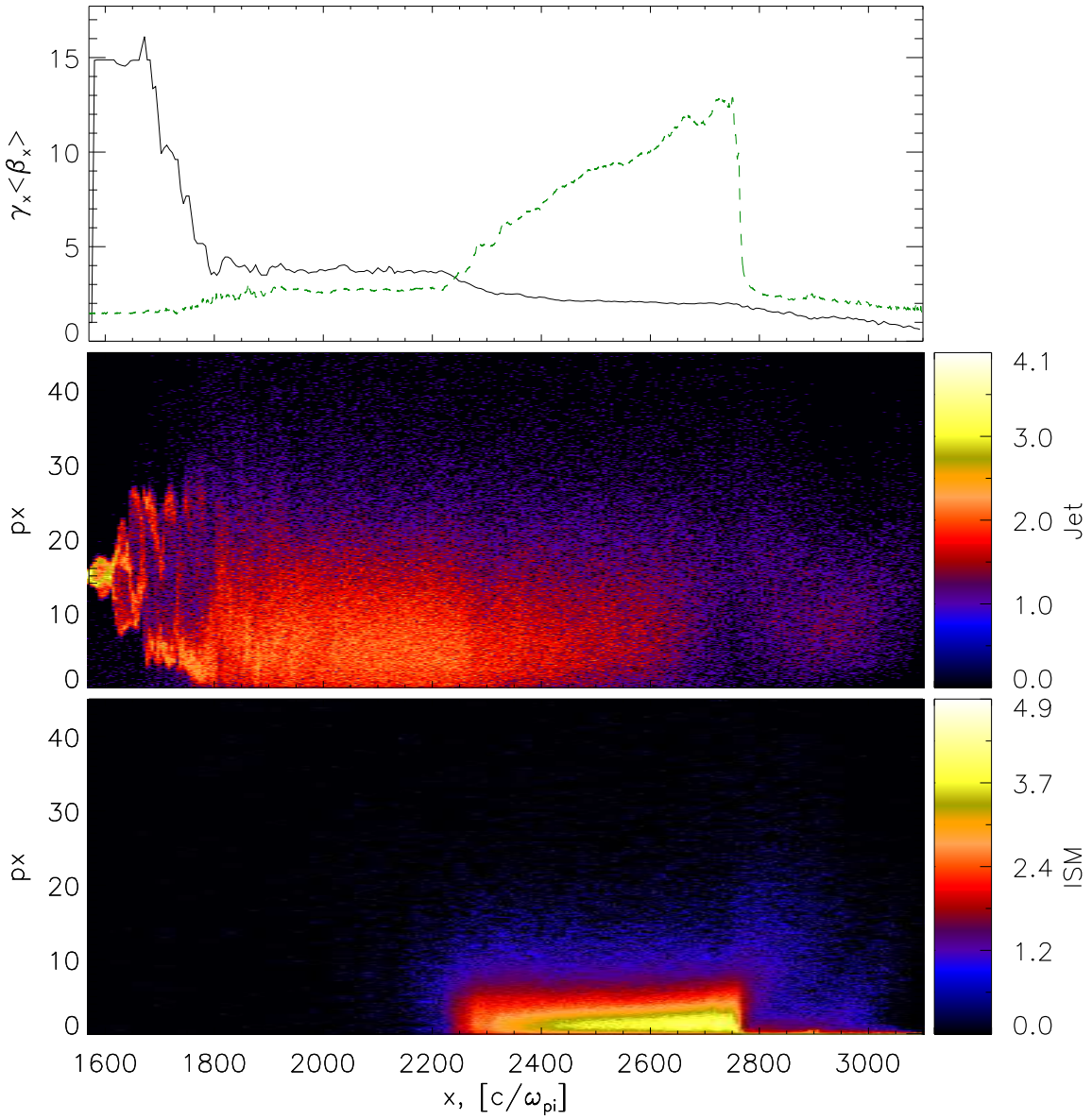

Figure 4.7: Profile of $\gamma_x < \beta_x >$ and phase space of a shock formed by a jet at $\gamma = 15$ colliding with a stationary plasma at the same density, at $\omega_p t = 3149$. Top panel: Profile of $\gamma_x < \beta_x >$ at each x-position where $\gamma_x = (1 - < \beta_x >^2)^{-1/2}$ (solid line), density profile (dashed line). Middle panel: Phase space for the jet particles. Bottom panel: Phase space for the ISM particles.

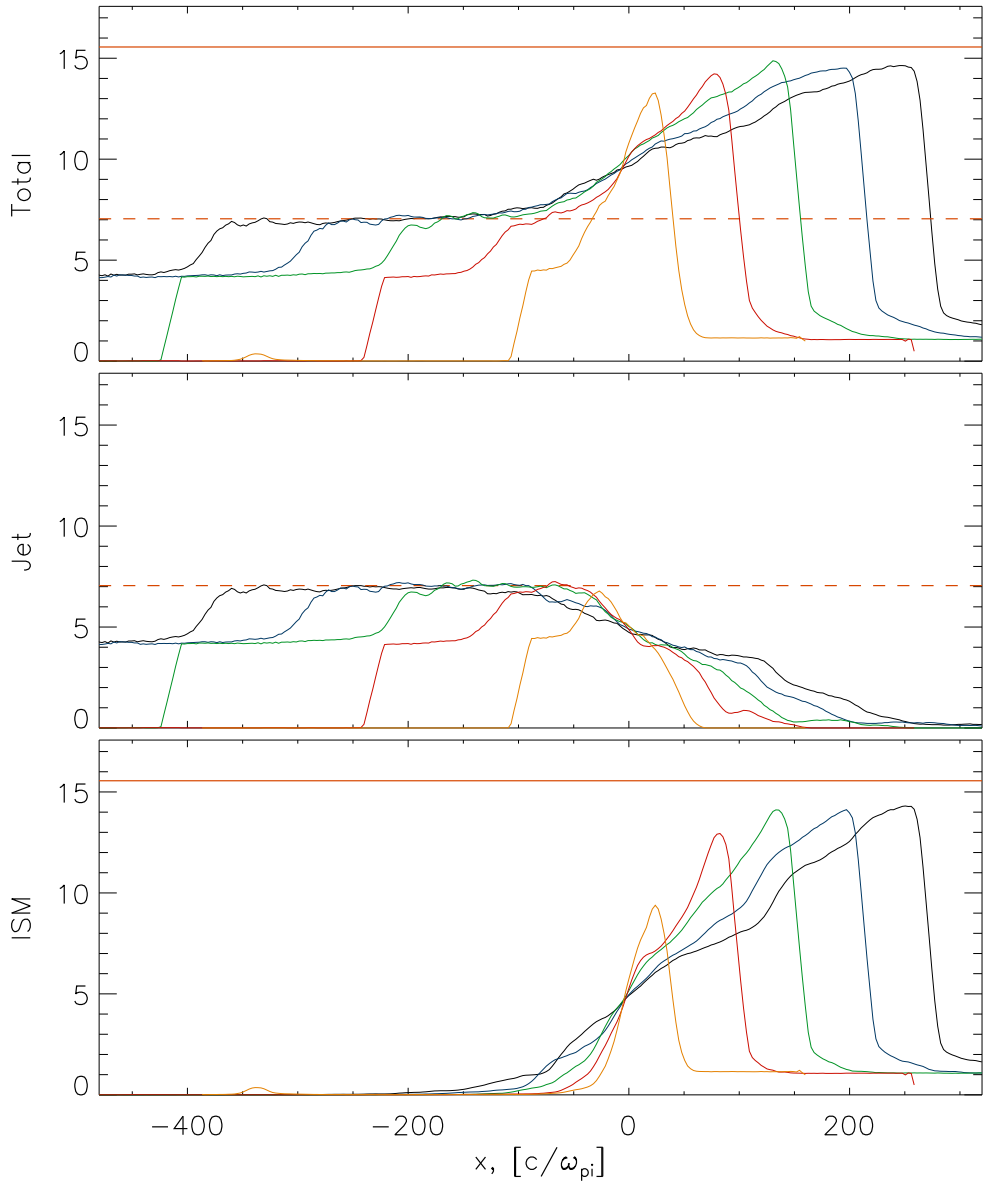

Figure 4.8: The evolution in density of a shock formed by a jet at $\gamma = 15$ colliding with a stationary plasma 4 times less dense, at $\omega_p t = 450$, 1125, 1800, 2475, and 3149. The orange lines indicate the predictions for density in the case of an ultrarelativistic reverse shock, where the prediction for the forward shock is solid and the prediction for the reverse shock is dashed. Top panel: Combined density. Middle panel: Jet density only. Bottom panel: ISM density only.

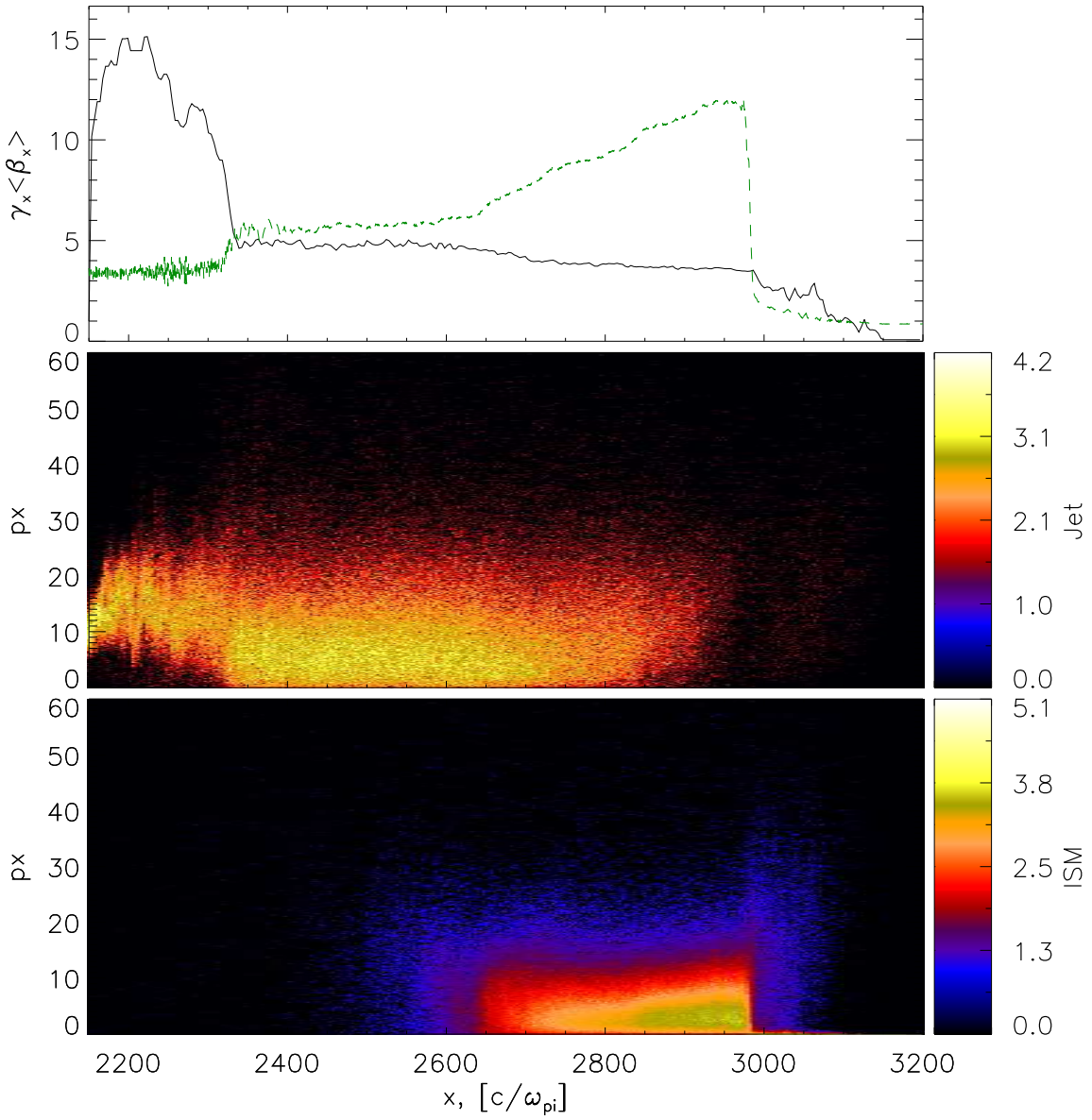

Figure 4.9: Profile of $\gamma_x < \beta_x >$ and phase space of a shock formed by a jet at $\gamma = 15$ colliding with a stationary plasma 4 times less dense, at $\omega_p t = 3149$. Top panel: Profile of $\gamma_x < \beta_x >$ at each x-position where $\gamma_x = (1 - < \beta_x >^2)^{-1/2}$ (solid line), density profile (dashed line). Middle panel: Phase space for the jet particles. Bottom panel: Phase space for the ISM particles.

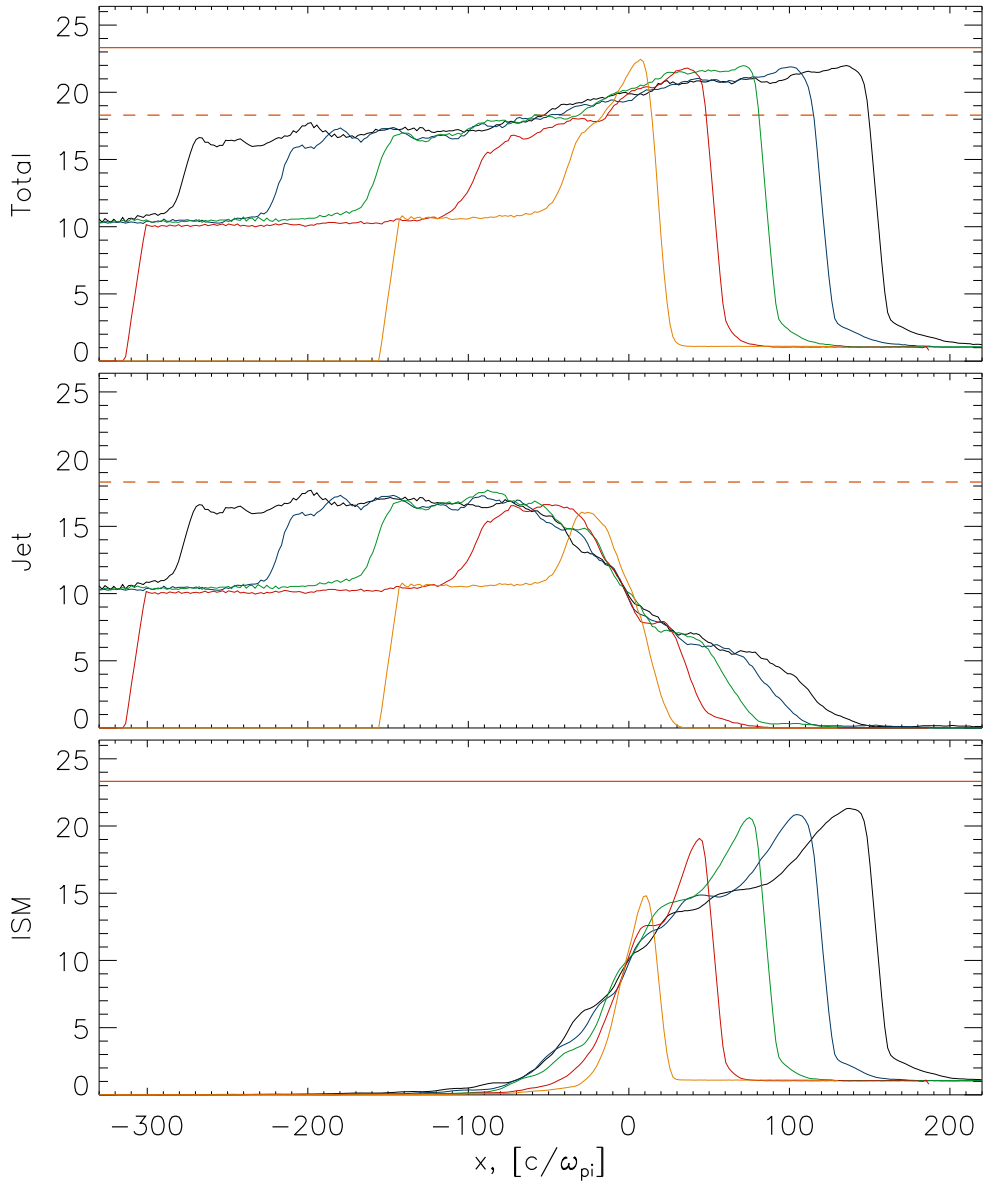

Figure 4.10: The evolution in density of a shock formed by a jet at $\gamma = 15$ colliding with a stationary plasma 10 times less dense, at $\omega_p t = 450$, 1079, 1709, 2340, and 2969. The orange lines indicate the predictions for density in the case of an ultrarelativistic reverse shock, where the prediction for the forward shock is solid and the prediction for the reverse shock is dashed. Top panel: Combined density. Middle panel: Jet density only. Bottom panel: ISM density only.

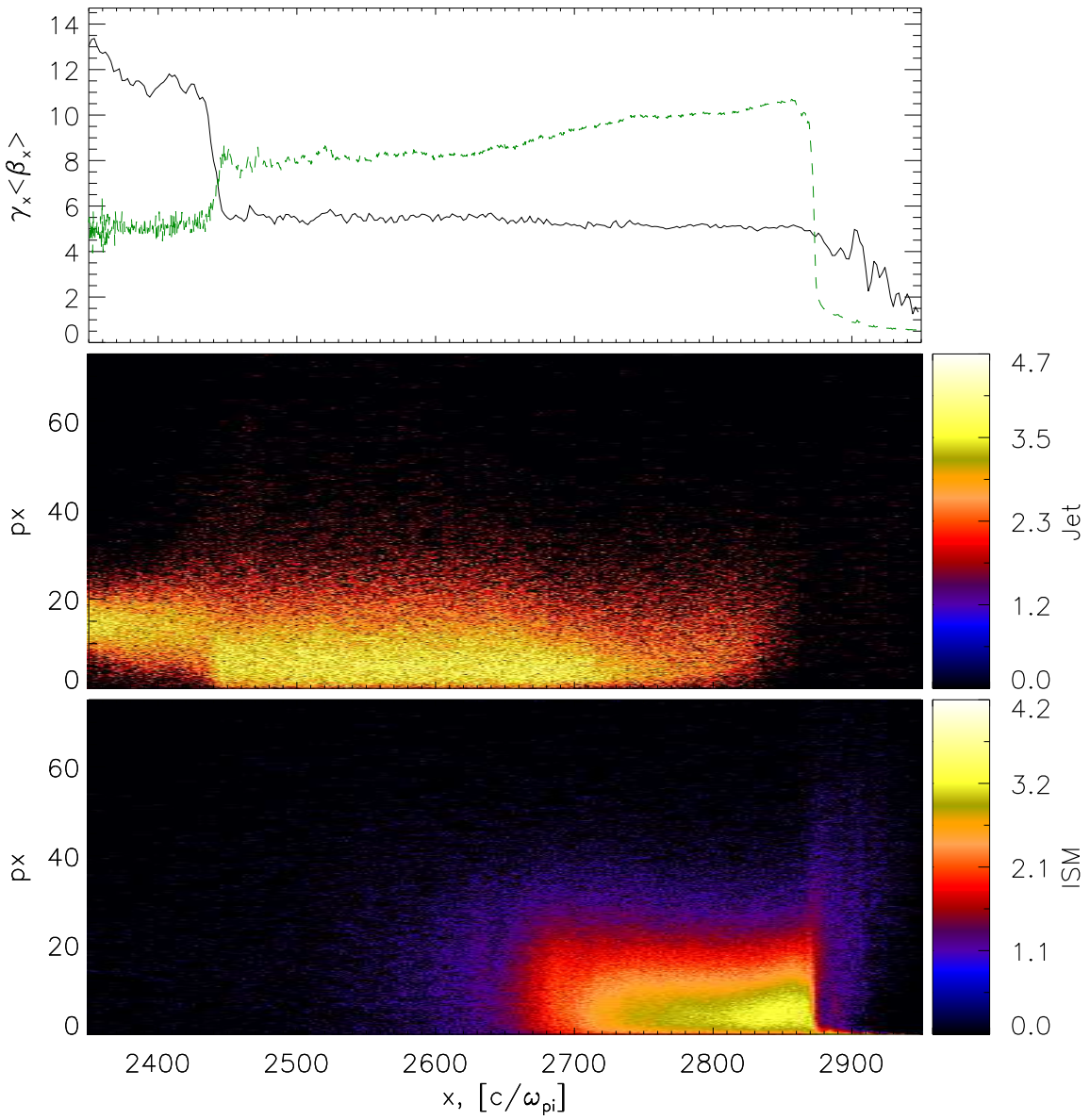

Figure 4.11: Profile of $\gamma_x < \beta_x >$ and phase space of a shock formed by a jet at $\gamma = 15$ colliding with a stationary plasma 10 times less dense, at $\omega_p t = 2969$. Top panel: Profile of $\gamma_x < \beta_x >$ at each x-position where $\gamma_x = (1 - < \beta_x >^2)^{-1/2}$ (solid line), density profile (dashed line). Middle panel: Phase space for the jet particles. Bottom panel: Phase space for the ISM particles.

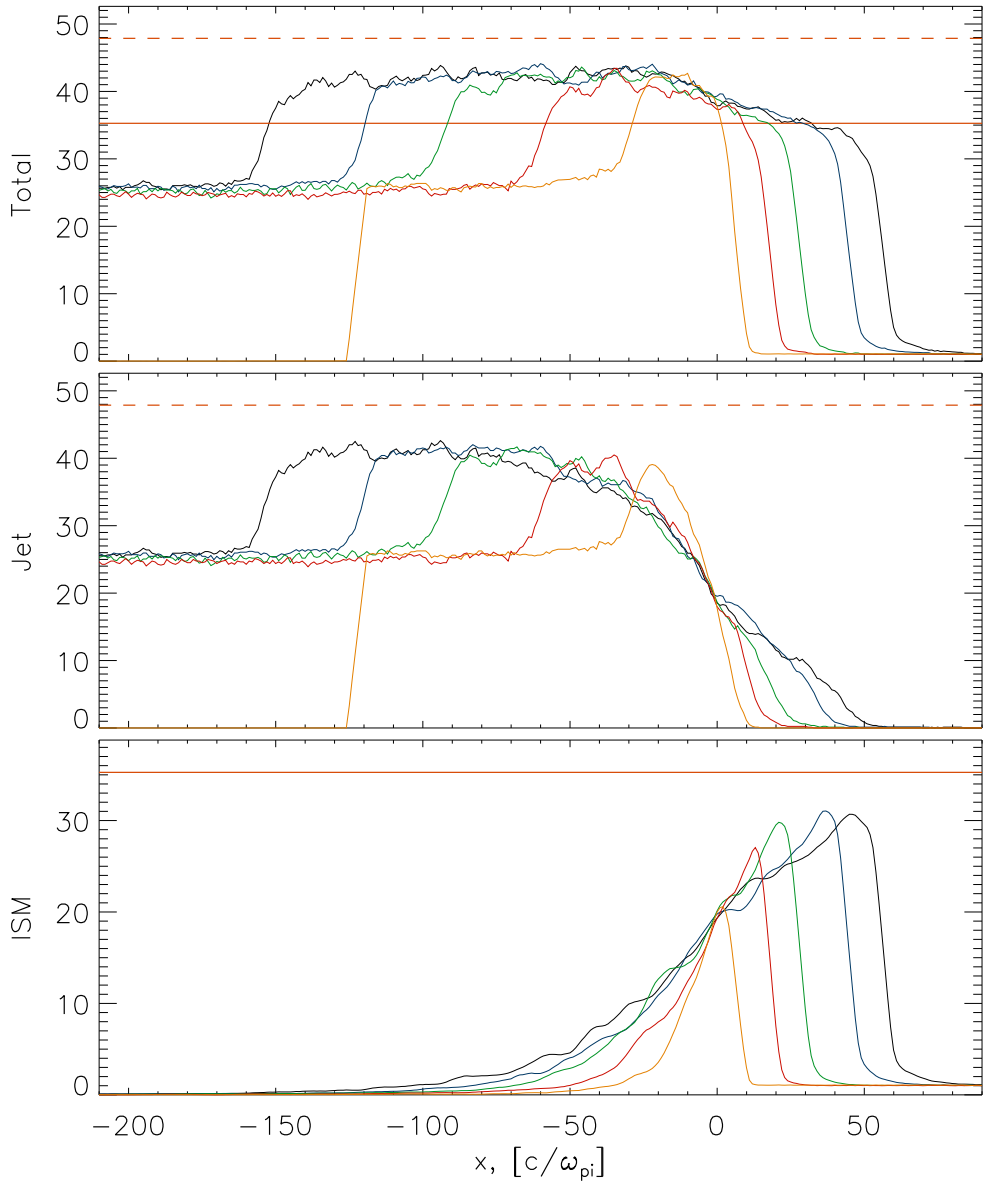

Figure 4.12: The evolution in density of a shock formed by a jet at $\gamma = 15$ colliding with a stationary plasma 25 times less dense, at $\omega_p t = 450$, 1125, 1800, 2475, and 3149. The orange lines indicate the predictions for density in the case of an ultrarelativistic reverse shock, where the prediction for the forward shock is solid and the prediction for the reverse shock is dashed. Top panel: Combined density. Middle panel: Jet density only. Bottom panel: ISM density only.

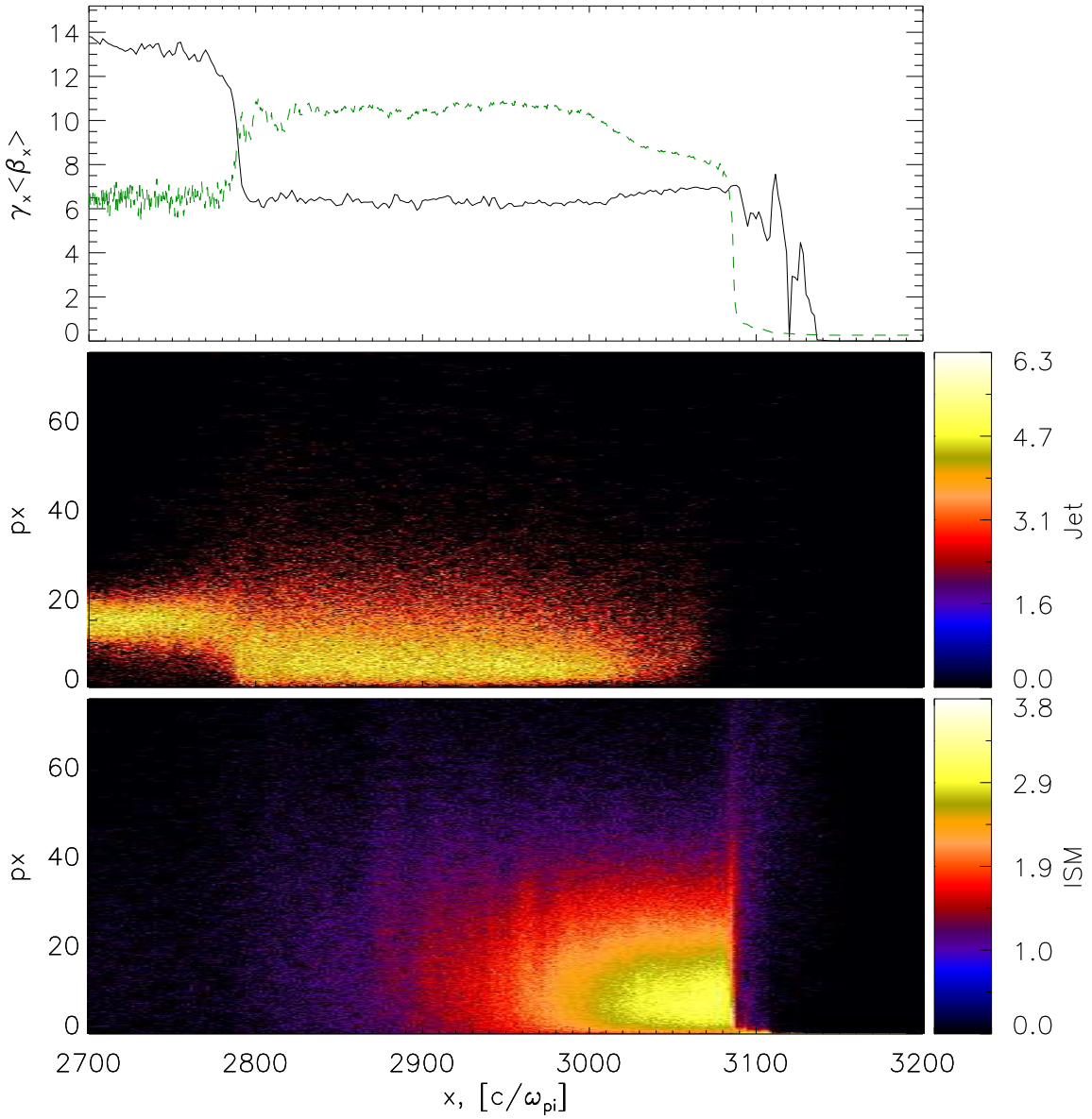

Figure 4.13: Profile of $\gamma_x < \beta_x >$ and phase space of a shock formed by a jet at $\gamma = 15$ colliding with a stationary plasma 25 times less dense, at $\omega_p t = 3149$. Top panel: Profile of $\gamma_x < \beta_x >$ at each x-position where $\gamma_x = (1 - < \beta_x >^2)^{-1/2}$ (solid line), density profile (dashed line). (Note: particle weighting produces noise in front of the forward shock.) Middle panel: Phase space for the jet particles. Bottom panel: Phase space for the ISM particles.

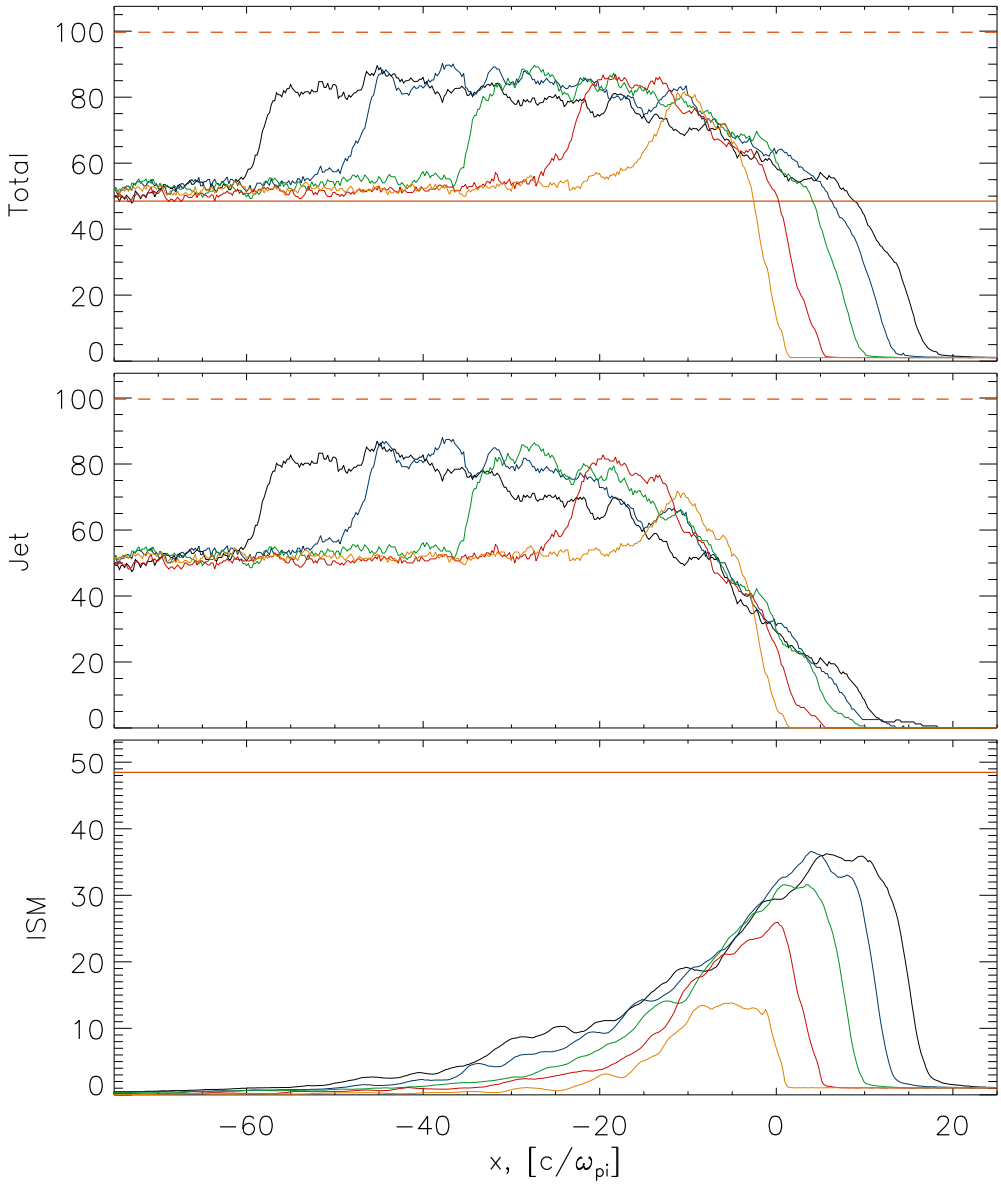

Figure 4.14: The evolution in density of a shock formed by a jet at $\gamma = 15$ colliding with a stationary plasma 50 times less dense, at $\omega_p t = 225$, 450, 674, 900, and 1125. The orange lines indicate the predictions for density in the case of an ultrarelativistic reverse shock, where the prediction for the forward shock is solid and the prediction for the reverse shock is dashed. Top panel: Combined density. Middle panel: Jet density only. Bottom panel: ISM density only.

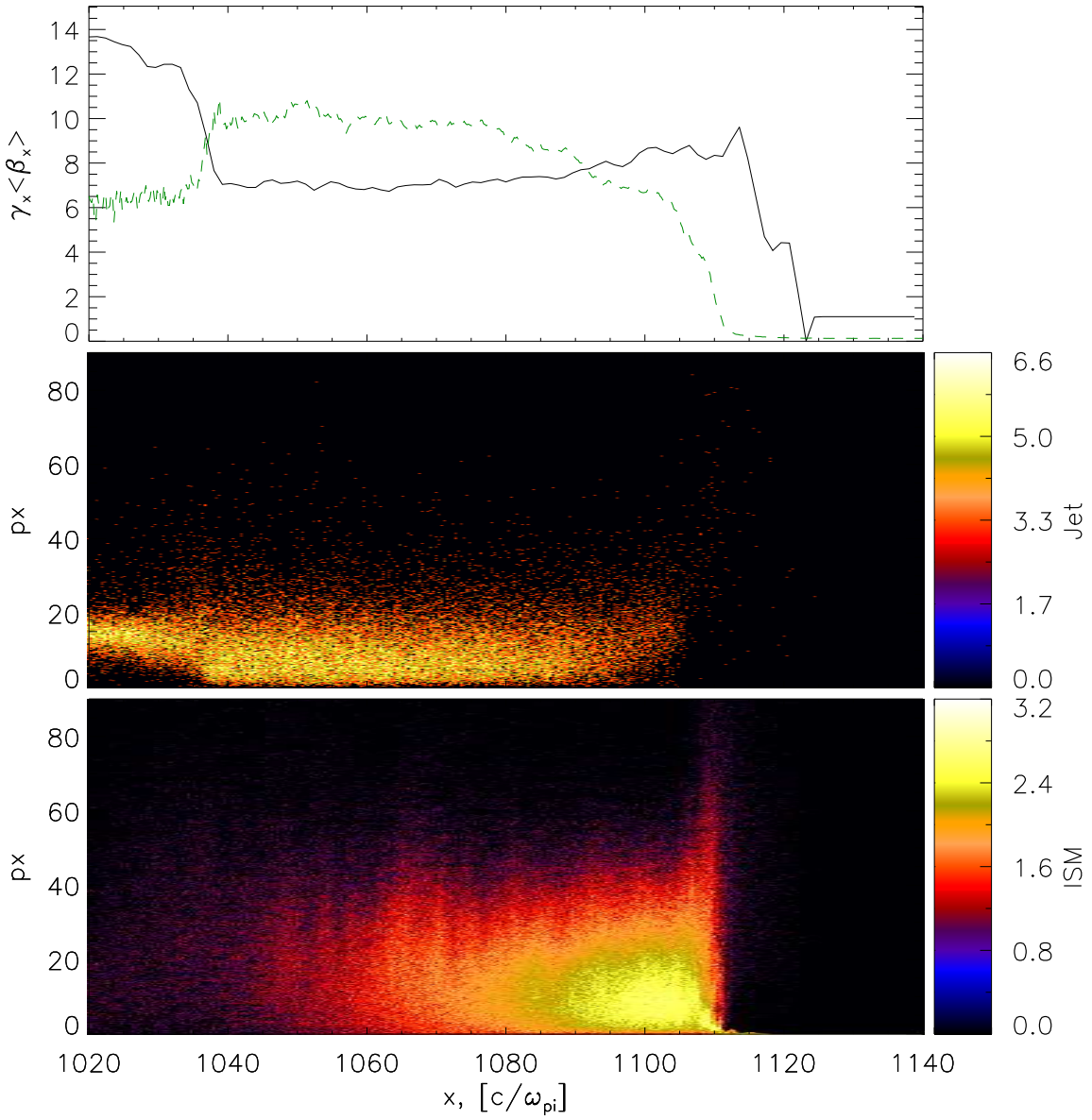

Figure 4.15: Profile of $\gamma_x < \beta_x >$ and phase space of a shock formed by a jet at $\gamma = 15$ colliding with a stationary plasma 50 times less dense, at $\omega_p t = 1125$. Top panel: Profile of $\gamma_x < \beta_x >$ at each x-position where $\gamma_x = (1 - < \beta_x >^2)^{-1/2}$ (solid line), density profile (dashed line). Middle panel: Phase space for the jet particles. Bottom panel: Phase space for the ISM particles.

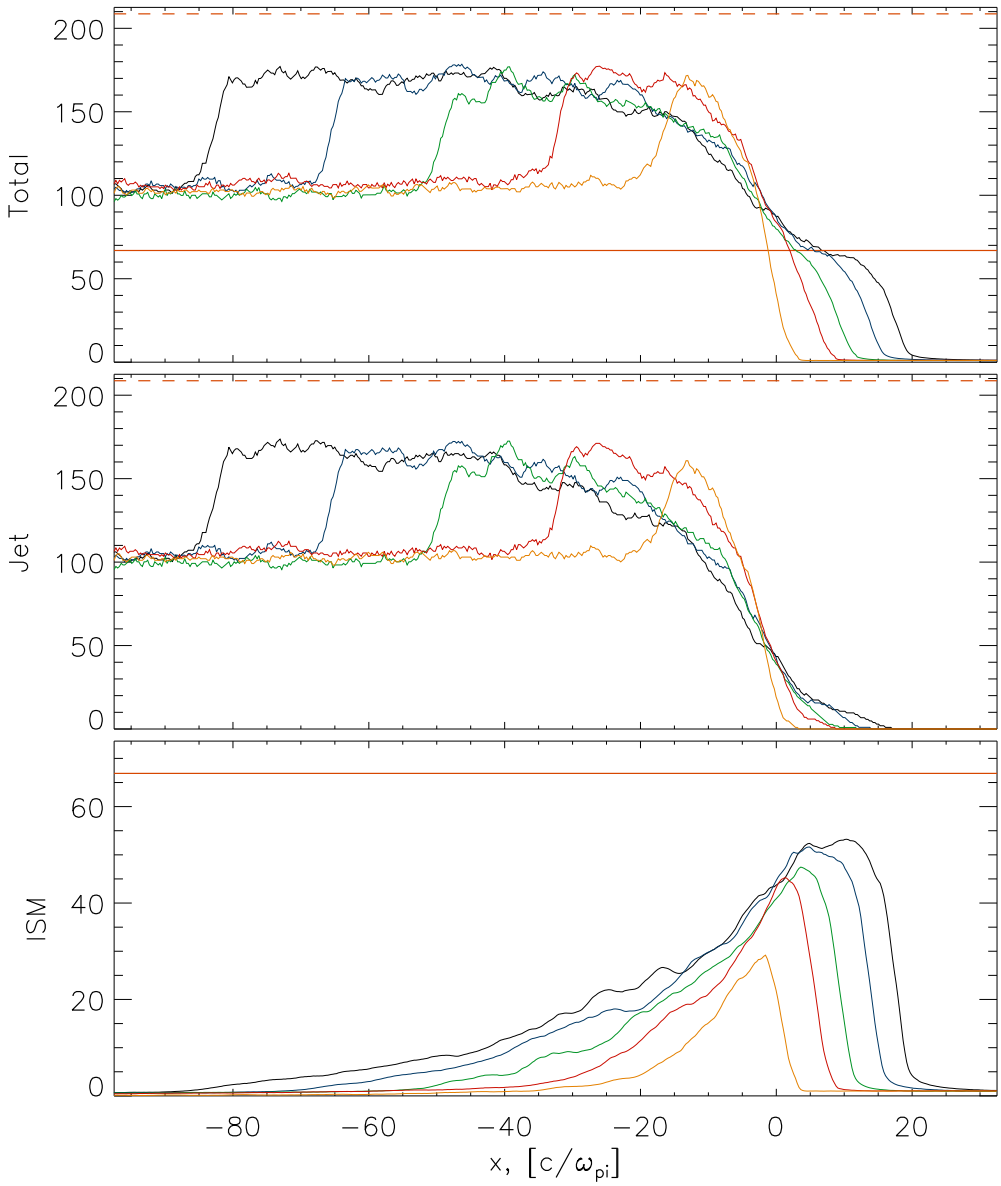

Figure 4.16: The evolution in density of a shock formed by a jet at $\gamma = 15$ colliding with a stationary plasma 100 times less dense, at $\omega_p t = 450$, 900, 1349, 1800, and 2250. The orange lines indicate the predictions for density in the case of an ultrarelativistic reverse shock, where the prediction for the forward shock is solid and the prediction for the reverse shock is dashed. Top panel: Combined density. Middle panel: Jet density only. Bottom panel: ISM density only (disregard black line).

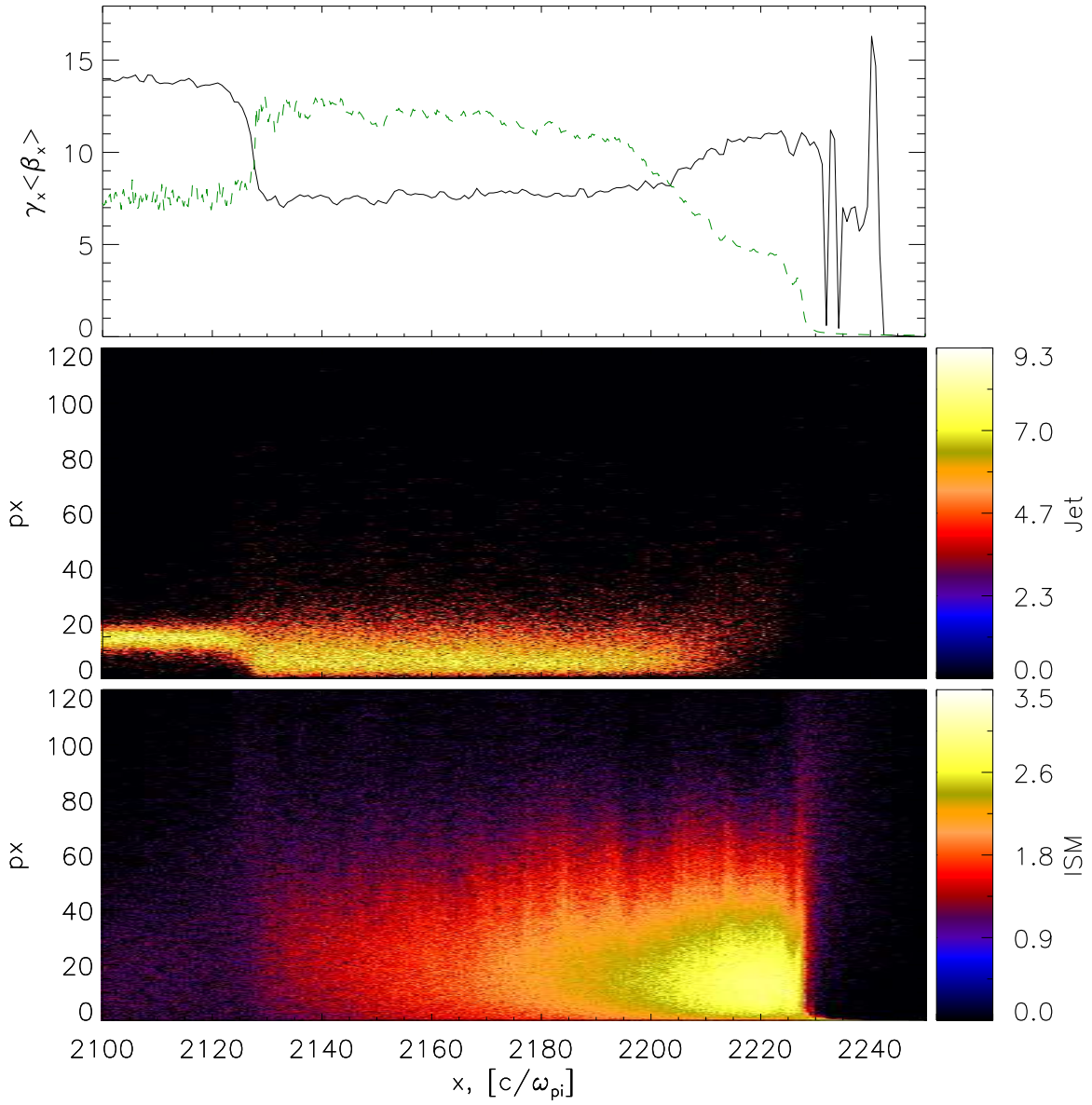

Figure 4.17: Profile of $\gamma_x < \beta_x >$ and phase space of a shock formed by a jet at $\gamma = 15$ colliding with a stationary plasma 100 times less dense, at $\omega_p t = 2250$. Top panel: Profile of $\gamma_x < \beta_x >$ at each x-position where $\gamma_x = (1 - < \beta_x >^2)^{-1/2}$ (solid line), density profile (dashed line). Middle panel: Phase space for the jet particles. Bottom panel: Phase space for the ISM particles.

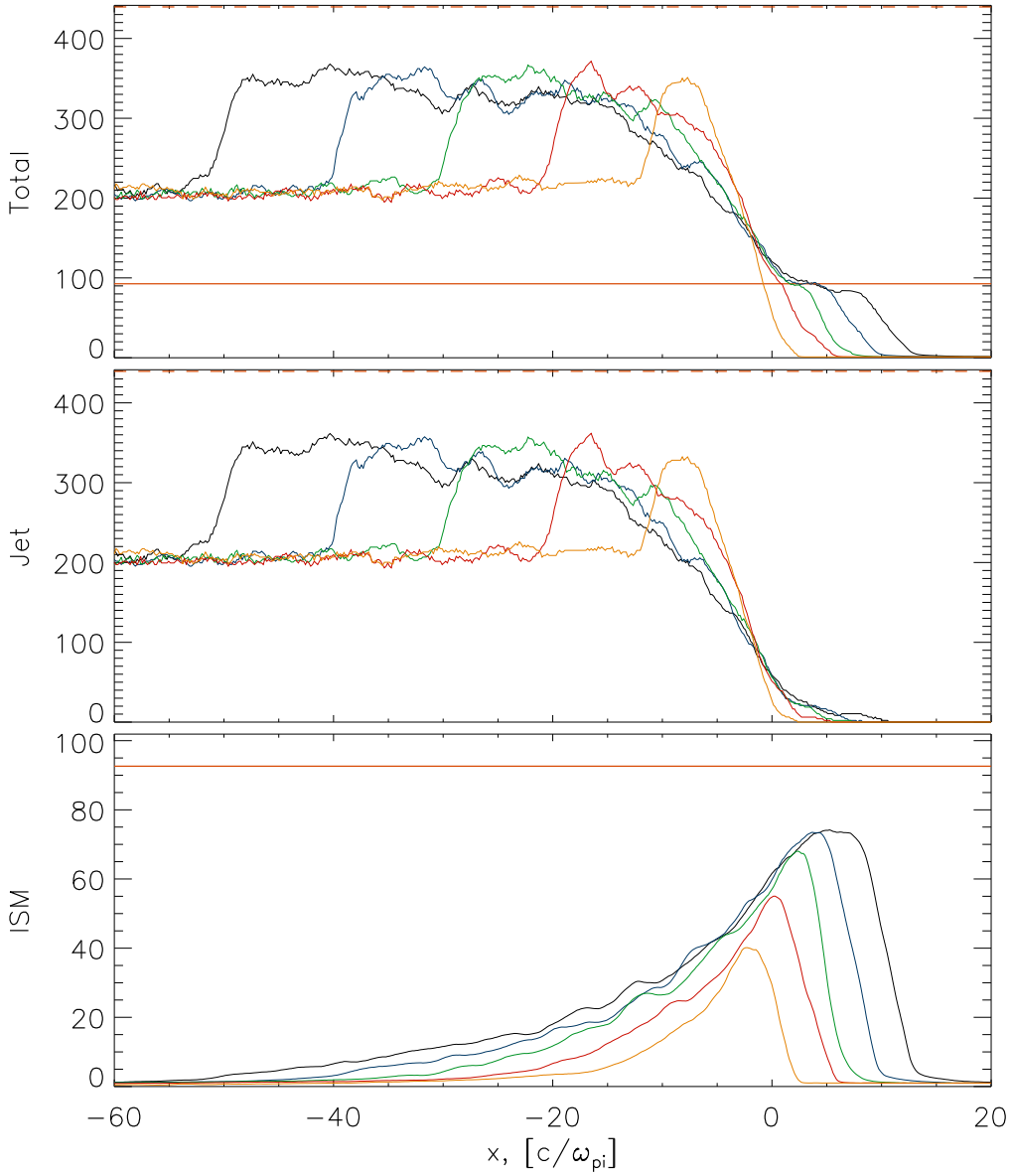

Figure 4.18: The evolution in density of a shock formed by a jet at $\gamma = 15$ colliding with a stationary plasma 200 times less dense, at $\omega_p t = 449$, 809, 1170, 1530, and 1890. The orange lines indicate the predictions for density in the case of an ultrarelativistic reverse shock, where the prediction for the forward shock is solid and the prediction for the reverse shock is dashed. Top panel: Combined density. Middle panel: Jet density only. Bottom panel: ISM density only (disregard black line).

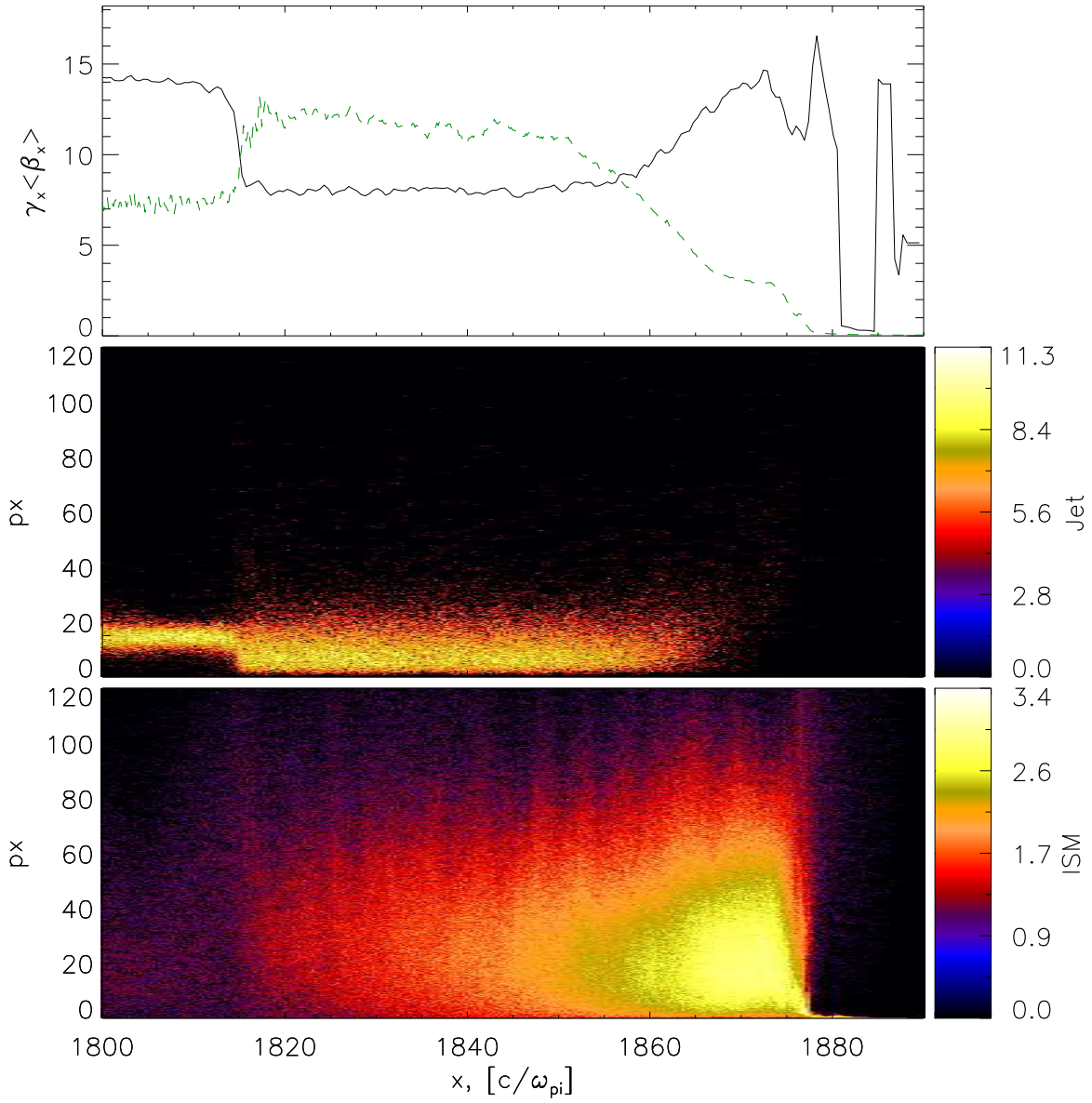

Figure 4.19: Profile of $\gamma_x < \beta_x >$ and phase space of a shock formed by a jet at $\gamma = 15$ colliding with a stationary plasma 200 times less dense, at $\omega_p t = 1890$. Top panel: Profile of $\gamma_x < \beta_x >$ at each x-position where $\gamma_x = (1 - < \beta_x >^2)^{-1/2}$ (solid line), density profile (dashed line). (Note: particle weighting produces noise in front of the forward shock.) Middle panel: Phase space for the jet particles. Bottom panel: Phase space for the ISM particles.

4.2.2 Magnetic Field Generation

In the jet-ISM shock scenario, magnetic fields are self-generated in two places: the forward shock and the reverse shock. These areas with strong magnetic fields affect the emission produced by accelerated particles (for example, by synchrotron emission). The magnitude of the magnetic field and the width of affected area contribute to this emission. Here we see how these fields evolve over time and compare the fields produced at the forward and reverse shocks. The top panel in Figures 4.20 through 4.26 shows the evolution (from the black lines to the yellow lines) of the density of magnetic energy generated by these shocks for the same density ratios as in the previous section (1:1, 1:4, 1:10, 1:25, 1:50, 1:100, and 1:200). The energy density plotted is normalized in the frame of the contact discontinuity by the kinetic energy of the upstream particles, so we can see what fraction of that energy contributes to the generation of the magnetic field at the forward shock..

First consider the case where the density ratio between the two plasmas is 1:1. The top panel of Figure 4.20 shows the z-component of the magnetic field energy density (B_z^2) at the forward and reverse shocks (the forward shock peak is on the right, the reverse shock on the left). For this case, the magnetic energy density at the reverse shock is much stronger, with a peak B_z^2 4-5 times higher. Additionally, the region at the reverse shock with magnetic field is wider, yielding much higher magnetic field energy density overall. At its peak, the energy density at the forward shock is roughly $15 - 20\%$ of the kinetic energy density. After the fields stabilize around the third timestep plotted, their shapes and magnitudes remain roughly constant.

Conversely, in the 200:1 case shown in the top panel of Figure 4.26, the peak magnetic field at the forward shock has overtaken the reverse shock and outstrips it in energy by nearly a factor of 2. It is still the case, however, that the magnetic field at the reverse shock covers a wider region than that at the forward shock. Because the forward shock region is so much narrower, their overall magnetic energies are

comparable, which was not the case in for the 1:1 shock. As in the previous case, once the magnetic fields are established, they stay roughly the same throughout the evolution of the shock.

As the density ratio between the two plasmas increases, a clear pattern emerges in the intermediate Figures 4.21 through 4.25. Those shocks with a higher density ratio between the jet and ISM plasmas produce a magnetic field at the forward shock with higher energy density relative to the reverse shock, though the fraction of upstream kinetic energy density that contributes to the formation of the forward shock magnetic field remains roughly $15-20\%$. In all cases, however, the magnetic field at the reverse shock covers a wider area than at the forward shock.

4.2.3 Particle Acceleration

Both the forward and reverse shocks in the jet-ISM scenario may acclerate particles to very high speeds across the shock fronts, as described in Section 1.2, by Fermi acceleration. Here we explore the efficiency of this acceleration and compare the accleration produced at the forward and reverse shocks for the same density ratios described in the previous sections (1:1, 4:1, 10:1, 25:1, 50:1, 100:1, and 200:1).

This acceleration is visible in the particle spectrum as the non-thermal tail on the high-gamma side of a Maxwellian distribution. The evolution of the particle spectra just behind the forward shock and reverse shock for each simulation are plotted in the bottom two panels of Figures 4.20 through 4.26, where the black line is the earliest timestep and the yellow line is the latest timestep plotted.

For the 1:1 density ratio shock whose spectra are shown in Figure 4.20, the Maxwellian peaks at γ slightly higher than 1 for the forward shock, and γ closer to 10 for the reverse shock. Particle acceleration is clearly visible at the forward shock, especially at later timesteps, in the non-thermal tail. As the density ratio increases, this tail in the forward shock spectrum lessens and eventually disappears.

For example, even in Figure 4.21 which shows a 4:1 shock, the tail is barely visible even at later timesteps.

At a density ratio of 200:1 (Figure 4.26, the non-thermal tail has disappeared in the forward shock, but is very clear in the reverse shock. Though not as strong as in this case, acceleration is also visible at the reverse shock in Figures 4.25 (100:1), 4.24 (50:1) and 4.23 (25:1), and a little bit in Figure 4.22 (10:1). It is clear that a higher density ratio between the two plasmas corresponds to stronger Fermi acceleration at the reverse shock, though at low density ratios particles may be accelerated in the forward shock as well.

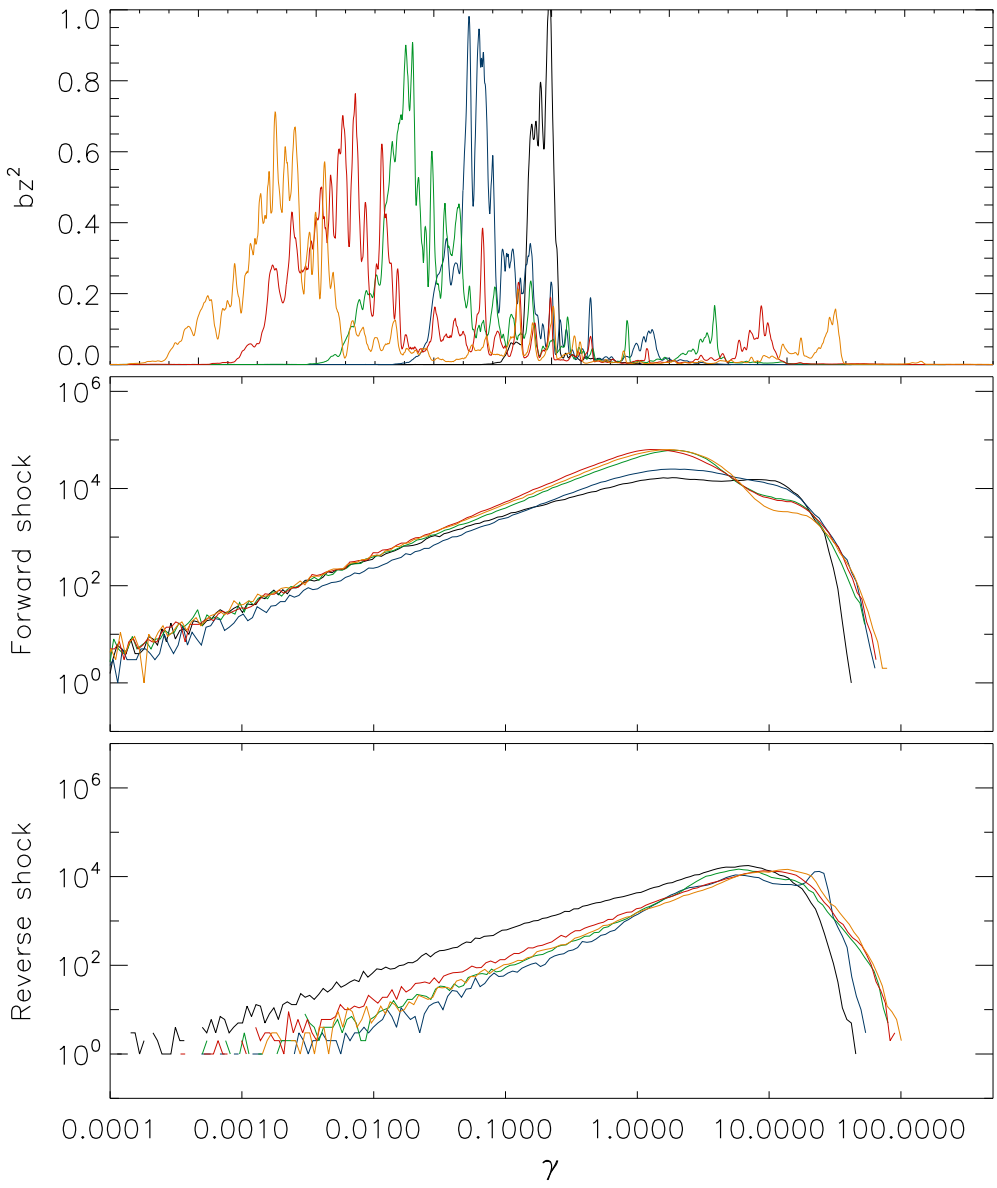

Figure 4.20: Magnetic field evolution and spectral evolution for a shock formed by a jet at $\gamma = 15$ colliding with a stationary plasma at the same density, at $\omega_p t = 450$, 1125, 1800, 2475, and 3149. Top panel: Square of the z-component of the magnetic field, normalized in the frame of the contact by the kinetic energy of the upstream. The leftmost peak is at the reverse shock, the rightmost peak at the forward shock. Middle panel: Particle spectrum just behind the forward shock. Bottom panel: Particle spectrum just behind the reverse shock.

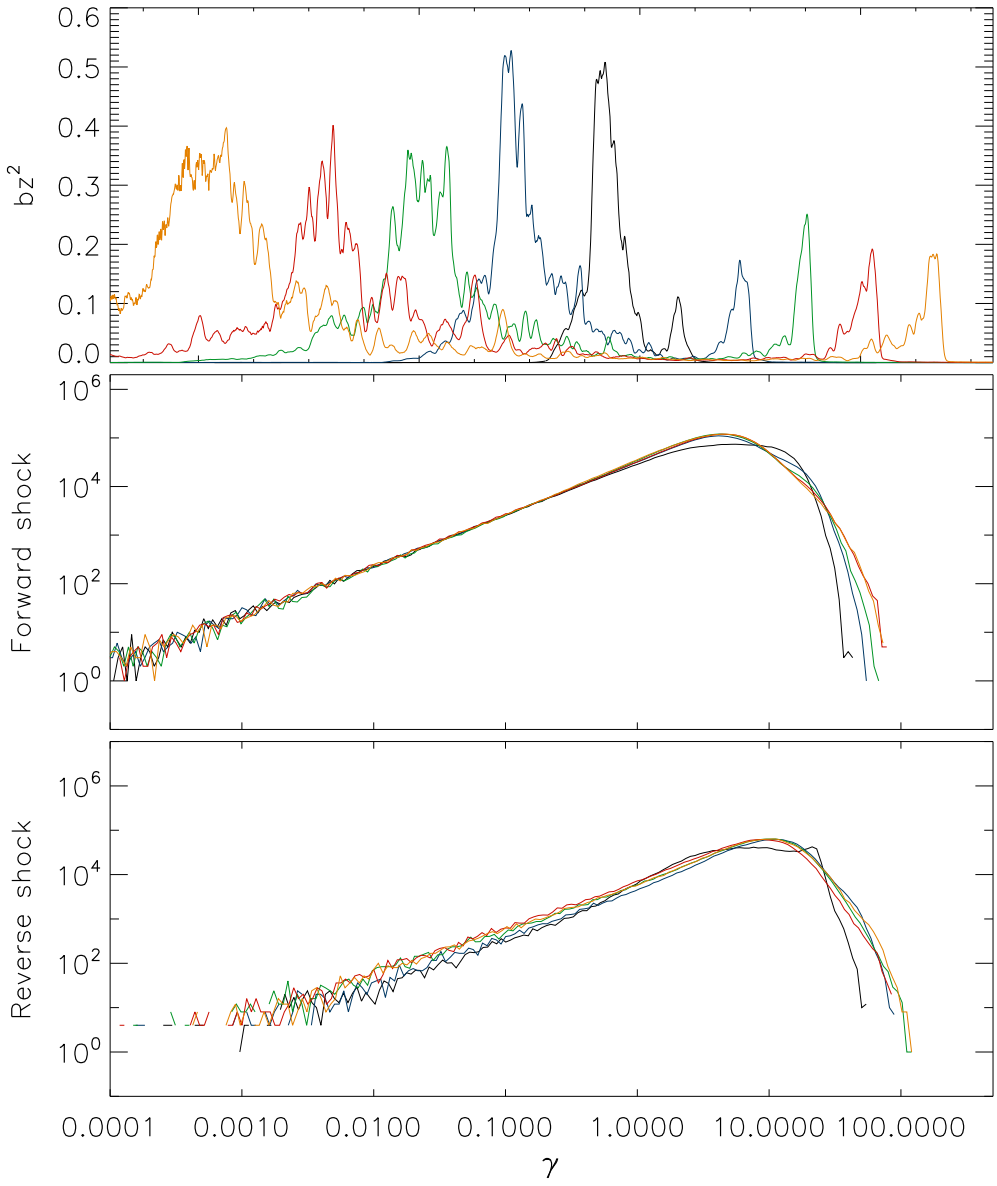

Figure 4.21: Magnetic field evolution and spectral evolution for a shock formed by a jet at $\gamma = 15$ colliding with a stationary plasma four times less dense, at $\omega_p t =$ 450, 1125, 1800, 2475, and 3149. Top panel: Square of the z-component of the magnetic field, normalized in the frame of the contact by the kinetic energy of the upstream. The leftmost peak is at the reverse shock, the rightmost peak at the forward shock. Middle panel: Particle spectrum just behind the forward shock. Bottom panel: Particle spectrum just behind the reverse shock.

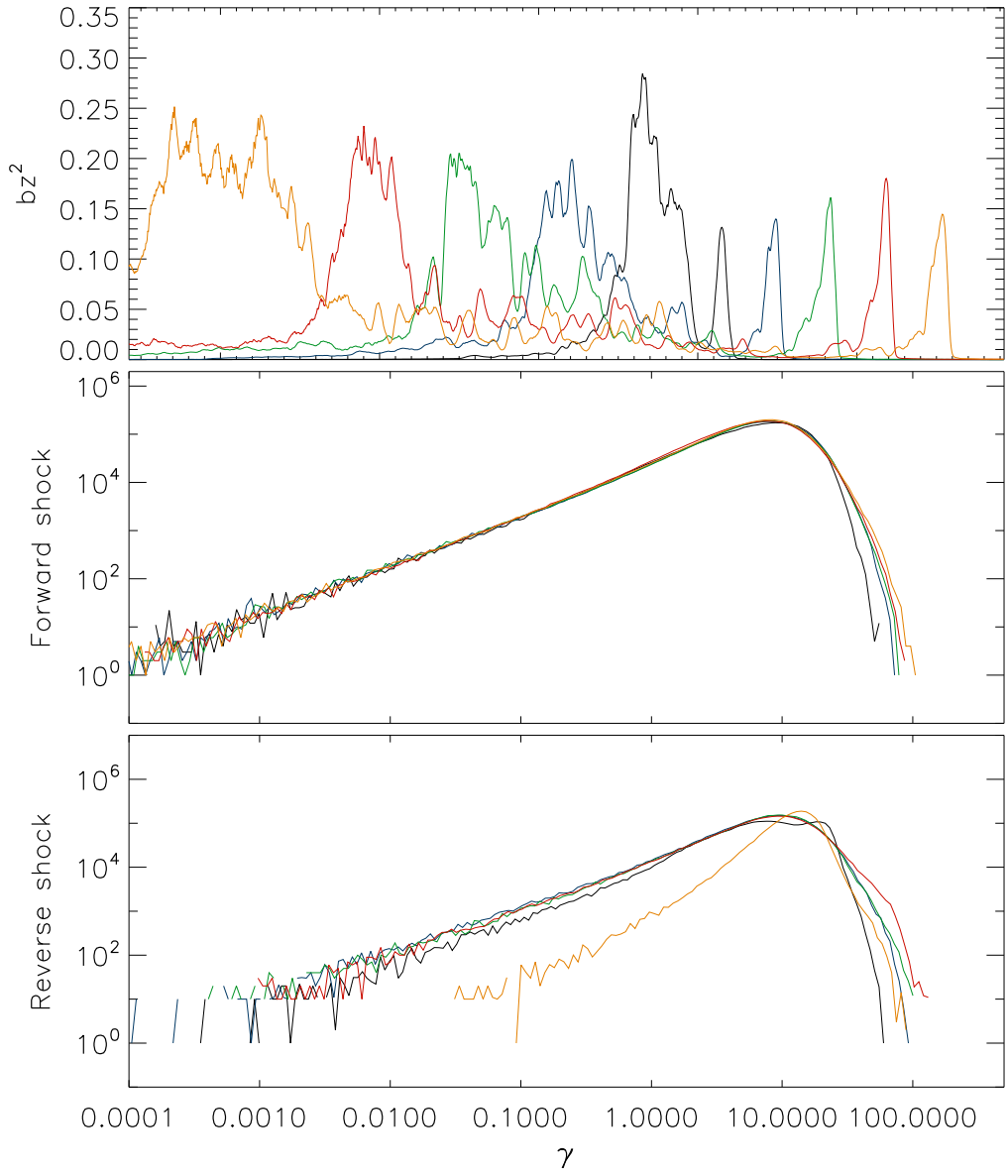

Figure 4.22: Magnetic field evolution and spectral evolution for a shock formed by a jet at $\gamma = 15$ colliding with a stationary plasma ten times less dense, at $\omega_p t =$ 450, 1079, 1709, 2340, and 2969. Top panel: Square of the z-component of the magnetic field, normalized in the frame of the contact by the kinetic energy of the upstream. The leftmost peak is at the reverse shock, the rightmost peak at the forward shock. Middle panel: Particle spectrum just behind the forward shock. Bottom panel: Particle spectrum just behind the reverse shock.

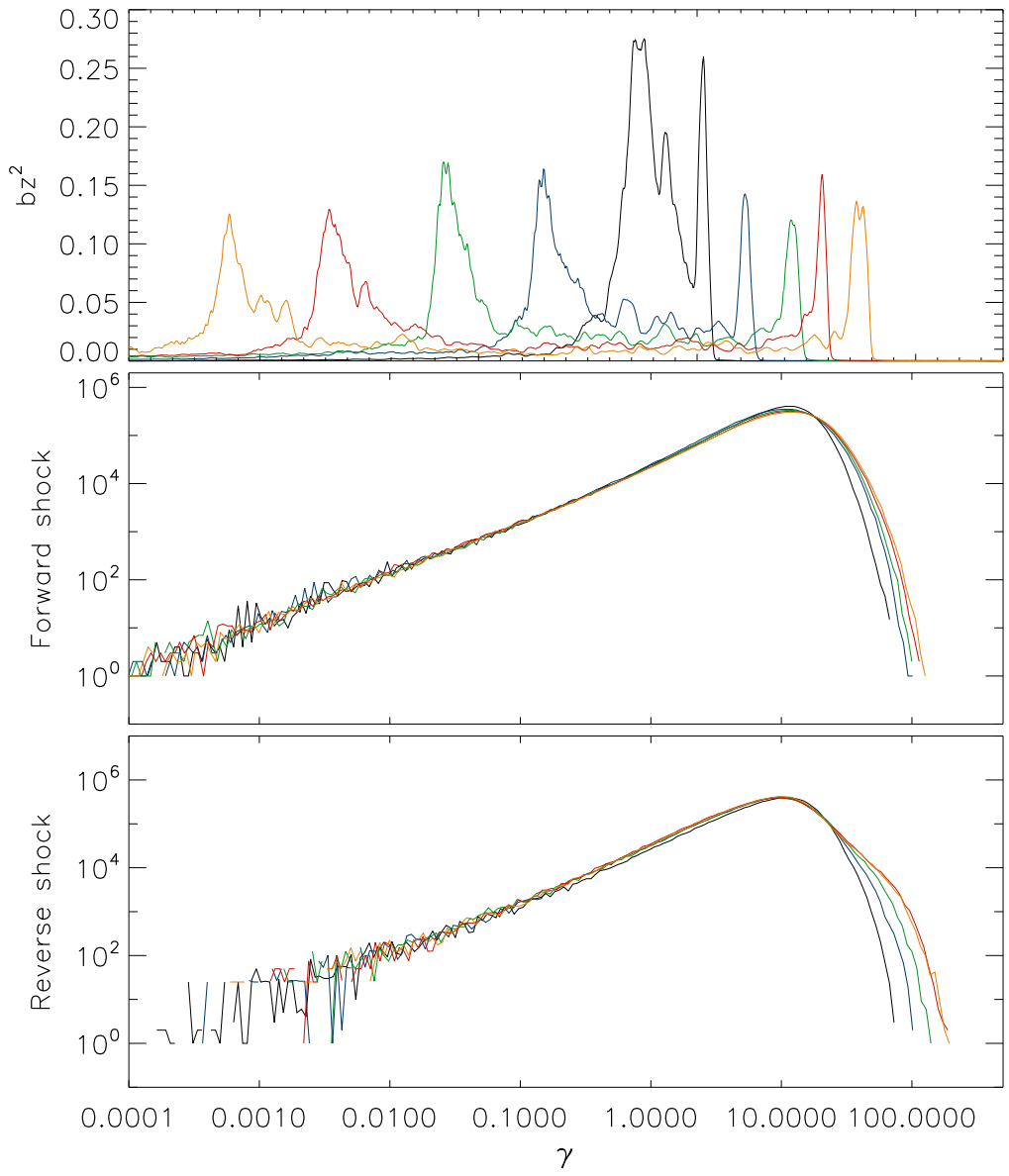

Figure 4.23: Magnetic field evolution and spectral evolution for a shock formed by a jet at $\gamma = 15$ colliding with a stationary plasma 25 times less dense, at $\omega_p t = 450$, 1125, 1800, 2475, and 3149. Top panel: Square of the z-component of the magnetic field, normalized in the frame of the contact by the kinetic energy of the upstream. The leftmost peak is at the reverse shock, the rightmost peak at the forward shock. Middle panel: Particle spectrum just behind the forward shock. Bottom panel: Particle spectrum just behind the reverse shock.

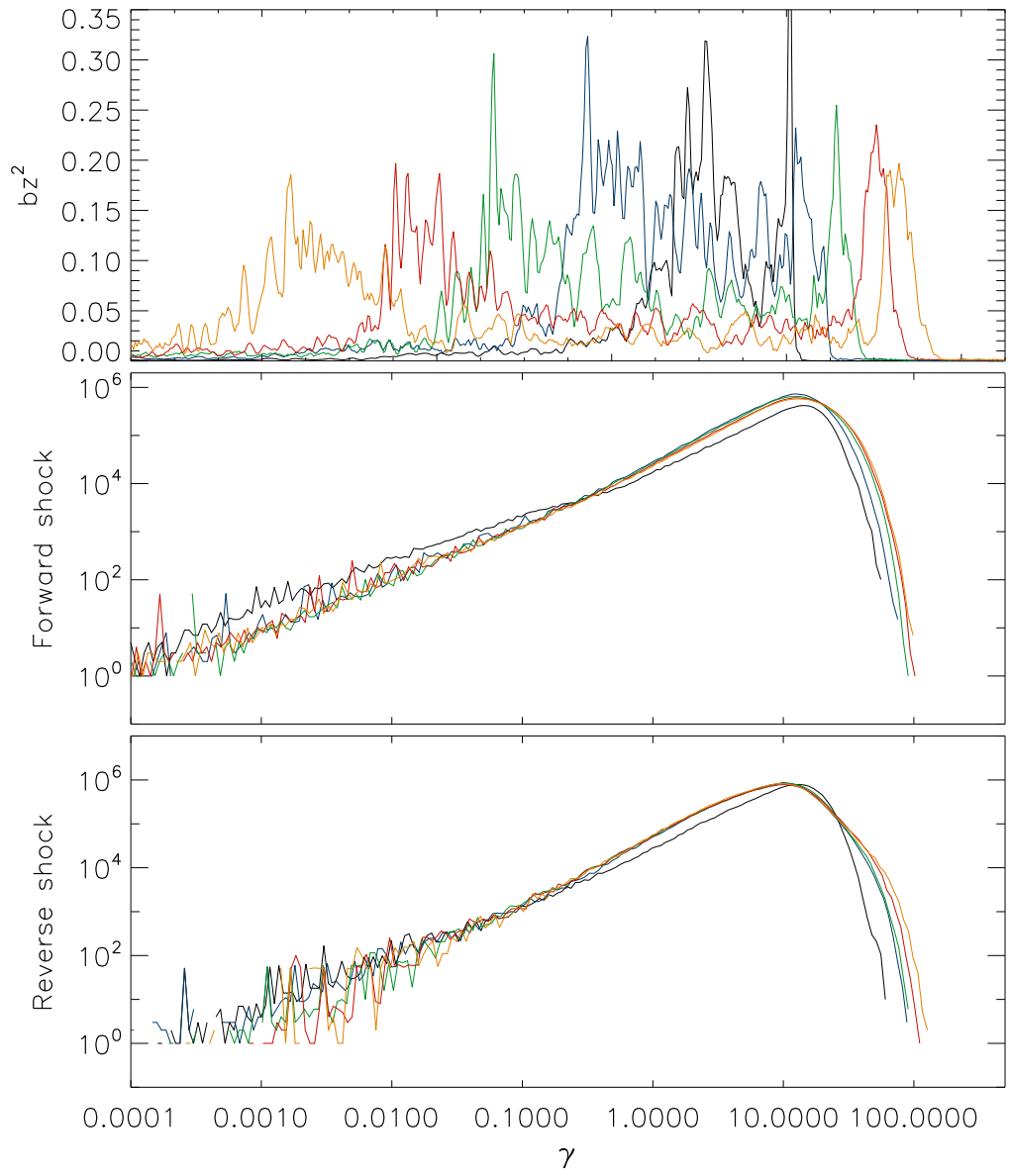

Figure 4.24: Magnetic field evolution and spectral evolution for a shock formed by a jet at $\gamma = 15$ colliding with a stationary plasma 50 times less dense, at $\omega_p t = 225$, 450, 674, 900, and 1125. Top panel: Square of the z-component of the magnetic field, normalized in the frame of the contact by the kinetic energy of the upstream. The leftmost peak is at the reverse shock, the rightmost peak at the forward shock. Middle panel: Particle spectrum just behind the forward shock. Bottom panel: Particle spectrum just behind the reverse shock.

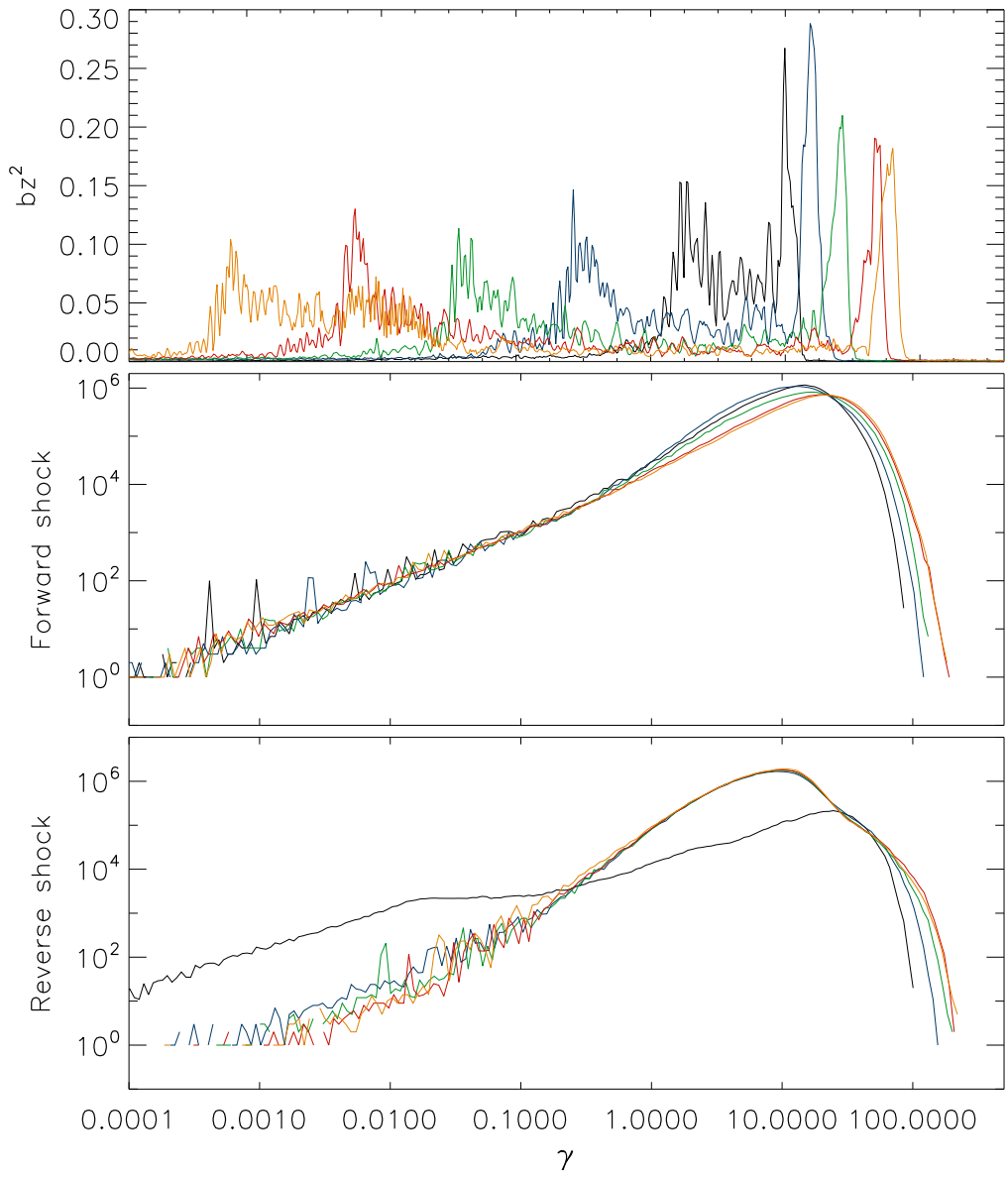

Figure 4.25: Magnetic field evolution and spectral evolution for a shock formed by a jet at $\gamma = 15$ colliding with a stationary plasma 100 times less dense, at $\omega_p t = 450$, 900, 1349, 1800, and 2250. Top panel: Square of the z-component of the magnetic field, normalized in the frame of the contact by the kinetic energy of the upstream. The leftmost peak is at the reverse shock, the rightmost peak at the forward shock. Middle panel: Particle spectrum just behind the forward shock. Bottom panel: Particle spectrum just behind the reverse shock.

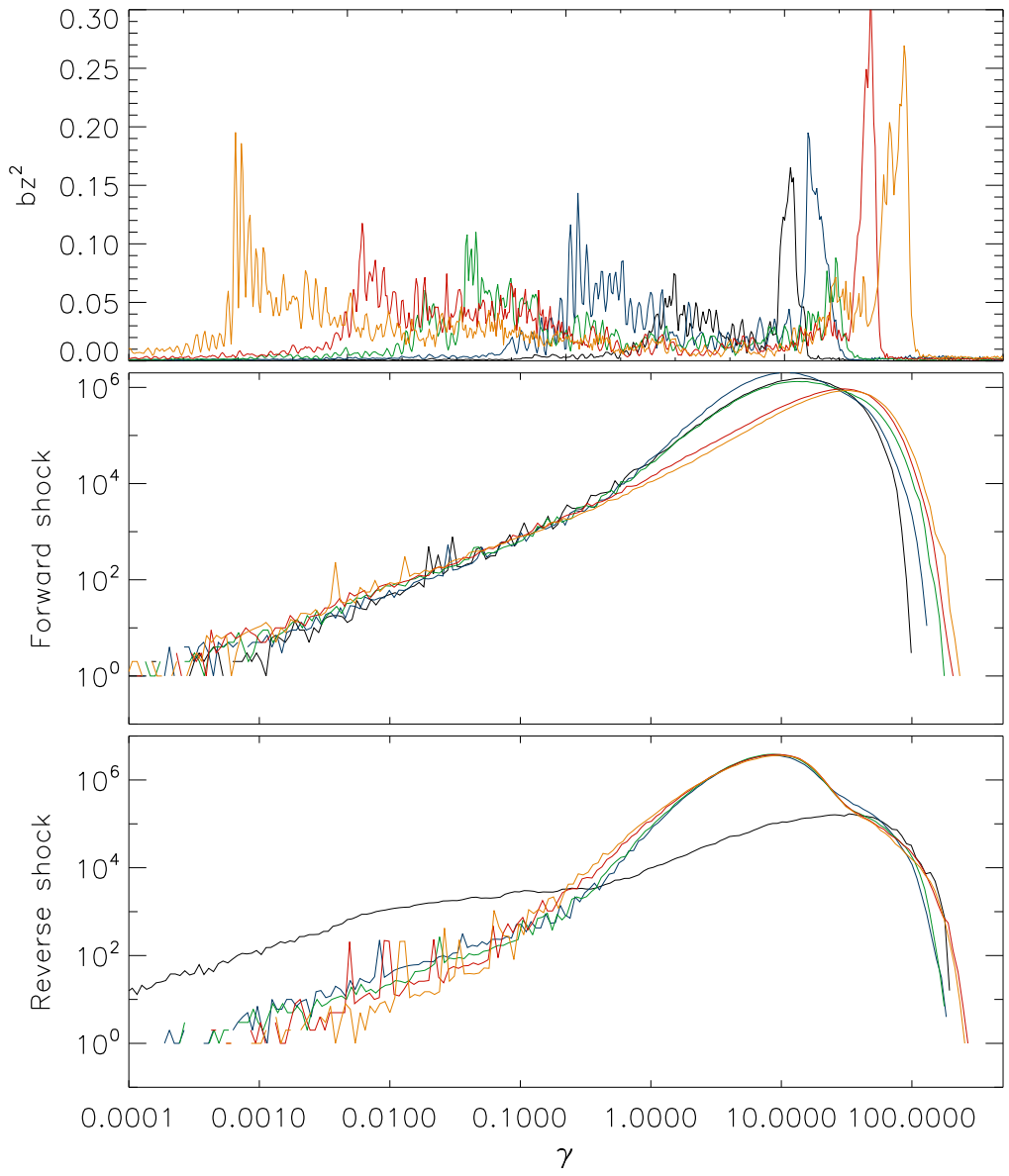

Figure 4.26: Magnetic field evolution and spectral evolution for a shock formed by a jet at $\gamma = 15$ colliding with a stationary plasma 200 times less dense, at $\omega_p t = 449$, 809, 1170, 1530, and 1890. Top panel: Square of the z-component of the magnetic field, normalized in the frame of the contact by the kinetic energy of the upstream. The leftmost peak is at the reverse shock, the rightmost peak at the forward shock. Middle panel: Particle spectrum just behind the forward shock. Bottom panel: Particle spectrum just behind the reverse shock.

Chapter 5

Radiation Spectra

From the particle and field data produced in the simulations in the previous chapter, we may predict the emission produced by the shocked particles as they travel through the magnetic fields generated at the forward and reverse shocks. In this chapter, we produce the radiation spectra of these shocks at several times throughout their evolution. Further, we decompose them into the emission produced separately at the forward and reverse shocks to determine which shock dominates the emission.

The code used to produce the radiation spectra, written by Lorenzo Sironi, uses the velocity and charge of a given particle as well as the magnetic field at its location to calculate the Lorentz force (and instantaneous acceleration) it experiences. It then uses this information to determine the energy spectrum produced by synchrotron radiation and sums the emission produced by the individual particles to produce an overall radiation spectrum.

The radiation spectra produced for the 4:1, 10:1, 25:1, 100:1, and 200:1 simulations presented in Section 4.2 are shown in Figures 5.1 to 5.5, where the y-axis is F_ν, the power at a given frequency in units which are arbitrary but consistent across the plots. In each plot, the black line is the total spectrum produced by the shocked particles, and it is decomposed into the contribution of the reverse shock (red) and

forward shock (blue).

In Figure 5.1, for example, the radiation spectrum is depicted at $\omega_p t = 450$, 1800, and 3149 (the first, third, and fifth times plotted in Figures 4.8 and 4.21). Here the reverse shock dominates emission at higher frequencies ($\gtrsim 20\ \omega/\omega_p$ in the first panel and decreasing with time), and the spectrum becomes increasingly dominated by the reverse shock as it evolves. At low frequency, the spectrum has a slope of 2/3 as expected for 2D synchrotron radiation. Although the spectrum widens somewhat with time to include higher frequencies, the location of the peak in ω/ω_p remains roughly constant, decreasing slightly between $\omega_p t = 450$ and 1800 and increasing between $\omega_p t = 1800$ and 3149. This stability reflects a compromise between the two emitting regions, as the location of the peak of the reverse shock spectrum shifts to higher ω/ω_p and the location of the peak of the forward shock spectrum decreases. The magnitude at the peak, however, rises by a factor of 6 over this time as the shocked region widens.

The spectrum produced by a 10:1 density ratio (Figure 5.2) tells a similar story, where the spectrum is dominated by the reverse shock with the peak power rising by a factor of 6 between $\omega_p t = 450$ and 2969. Again, ω/ω_p at the peak remains roughly constant, shifting from 60 to 42 to 70 in the first, second, and third panels respectively while the spectrum widens to higher frequencies.

For the 25:1 and 100:1 cases (Figures 5.3 and 5.4), the power emitted at very high frequencies is actually dominated by the forward shock although the spectrum overall is dominated by the reverse shock. In some cases, this is caused by a shallower slope after the peak for the forward shock emission, and in some cases it occurs because the "break," or change in slope, occurs at higher frequency for the forward shock spectrum than the reverse shock spectrum.

Finally, looking at the radiation spectrum produced by a 200:1 density ratio shock (Figure 5.5) in comparison to the 4:1 spectrum, it is clear that the emission is both

more luminous at the peak ($F_{\nu,peak}$ is roughly 75 times higher in the 200:1 case at comparable $\omega_p t$) and harder, extending to higher frequencies. The relative positions of the forward and reverse shock peaks have shifted as well; in the 4:1 case the reverse shock spectrum peaks at higher frequency than the forward shock spectrum, but the opposite is true in the 200:1 case.

Overall, the radiation spectra follow the same kind of patterns observed for the particle spectra in Section 4.2.3. Just as particle acceleration was stronger for high density ratios, so is the radiation spectrum more luminous. Similarly, the higher peak in γ in the forward shock particle spectrum for the high density ratio case manifests itself as a higher-frequency peak in the radiation spectrum. Most importantly, the particle acceleration was much stronger at the reverse shock than the forward shock, and so we find that the radiation spectra are dominated by emission produced at the reverse shock.

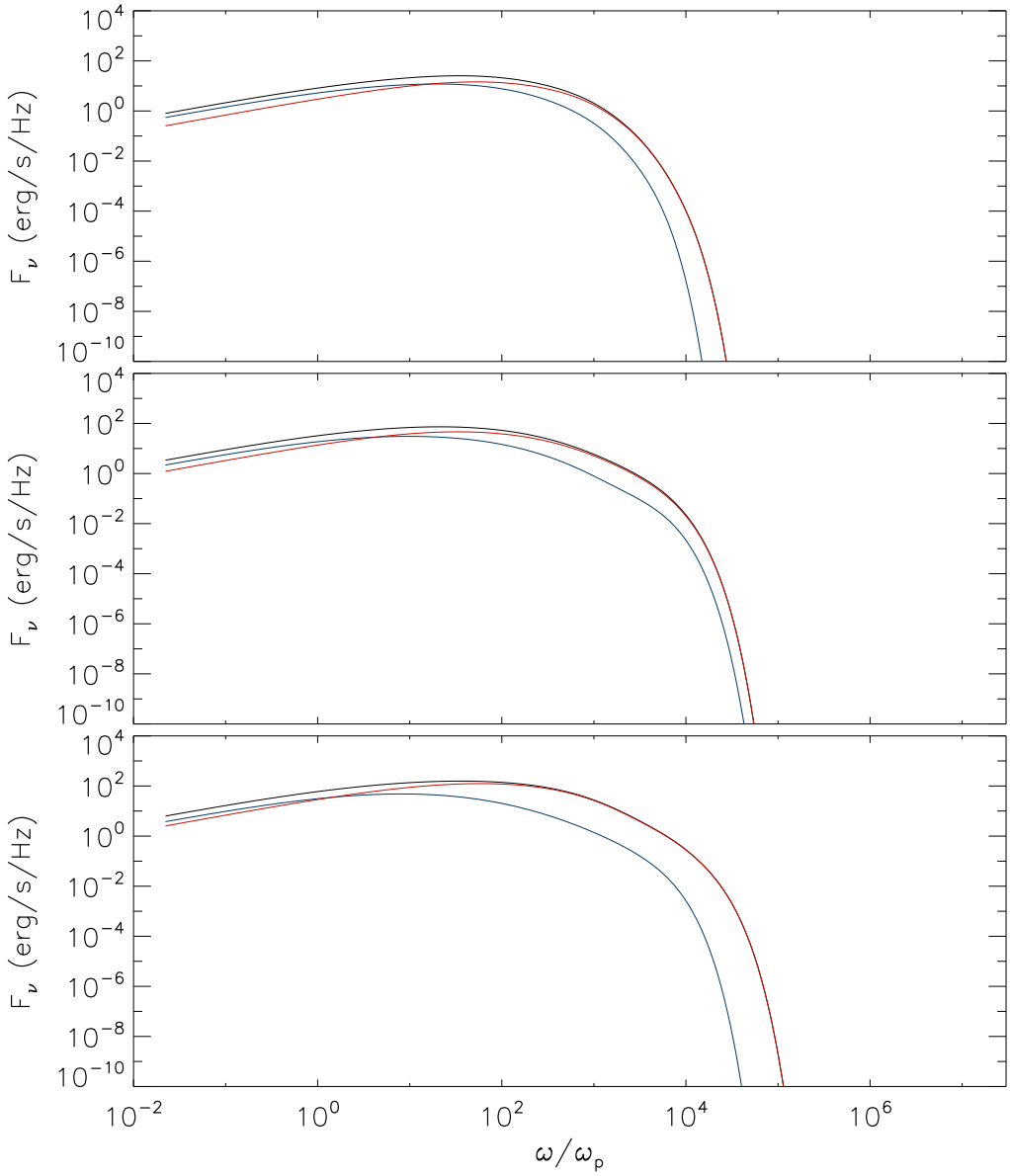

Figure 5.1: Radiation spectrum produced by a shock at a density ratio 4:1, at $\omega_p t =$ 450 (top), 1800 (middle), and 3149 (bottom). Red lines: Reverse shock spectrum. Blue lines: Forward shock spectrum. Black lines: Combined spectrum.

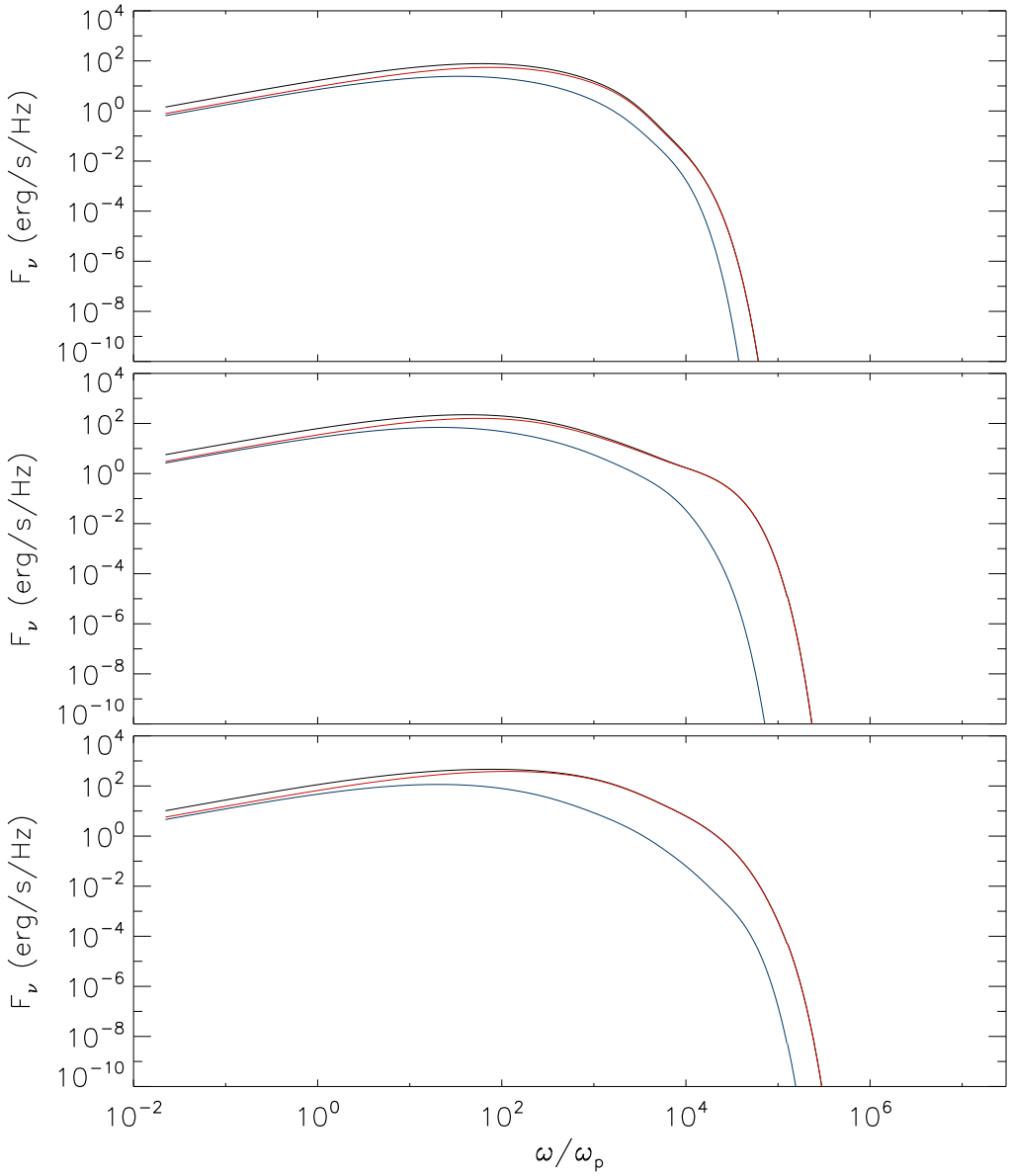

Figure 5.2: Radiation spectrum produced by a shock at a density ratio 10:1, at $\omega_p t =$ 450 (top), 1709 (middle), and 2969 (bottom). Red lines: Reverse shock spectrum. Blue lines: Forward shock spectrum. Black lines: Combined spectrum.

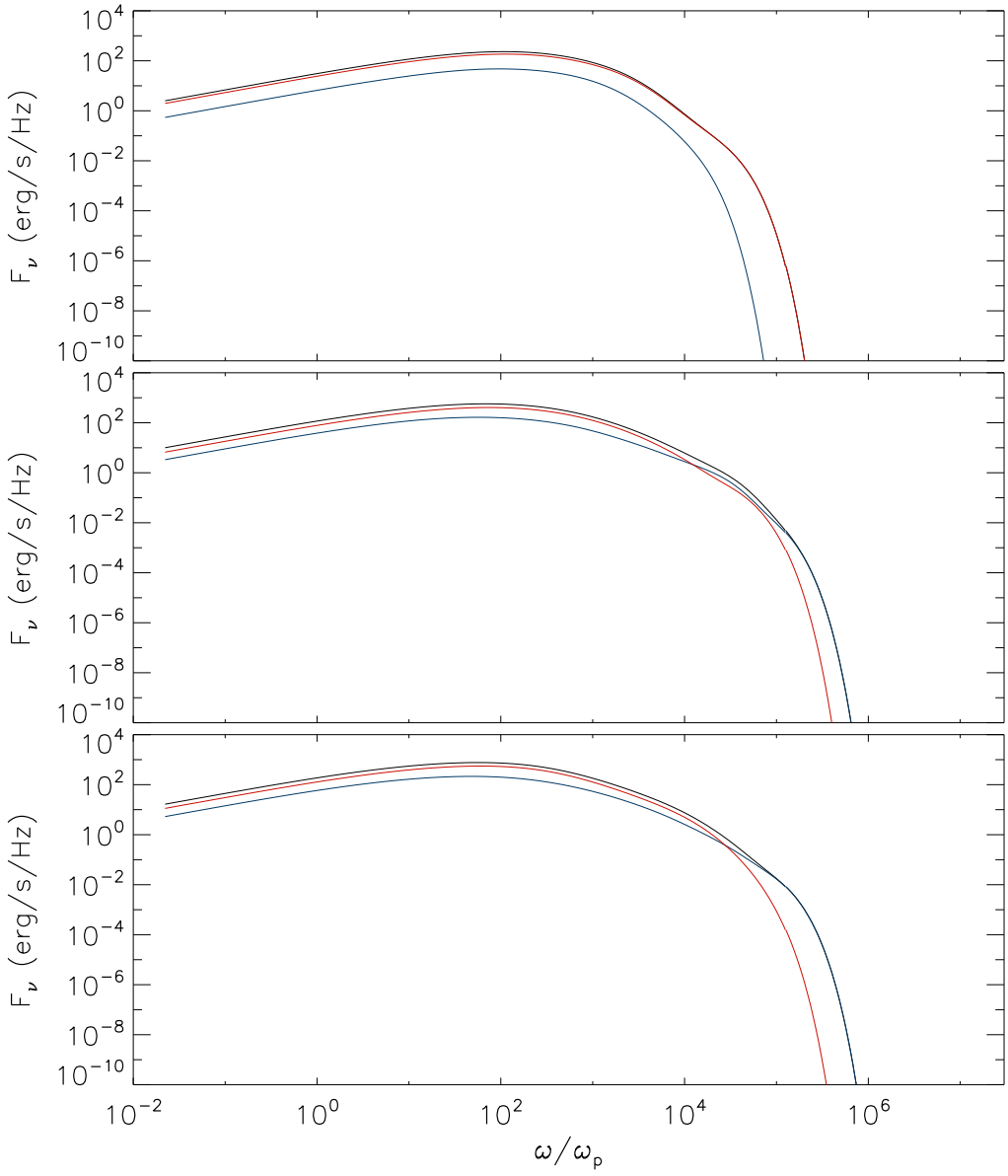

Figure 5.3: Radiation spectrum produced by a shock at a density ratio 25:1, at $\omega_p t =$ 450 (top), 1800 (middle), and 3149 (bottom). Red lines: Reverse shock spectrum. Blue lines: Forward shock spectrum. Black lines: Combined spectrum.

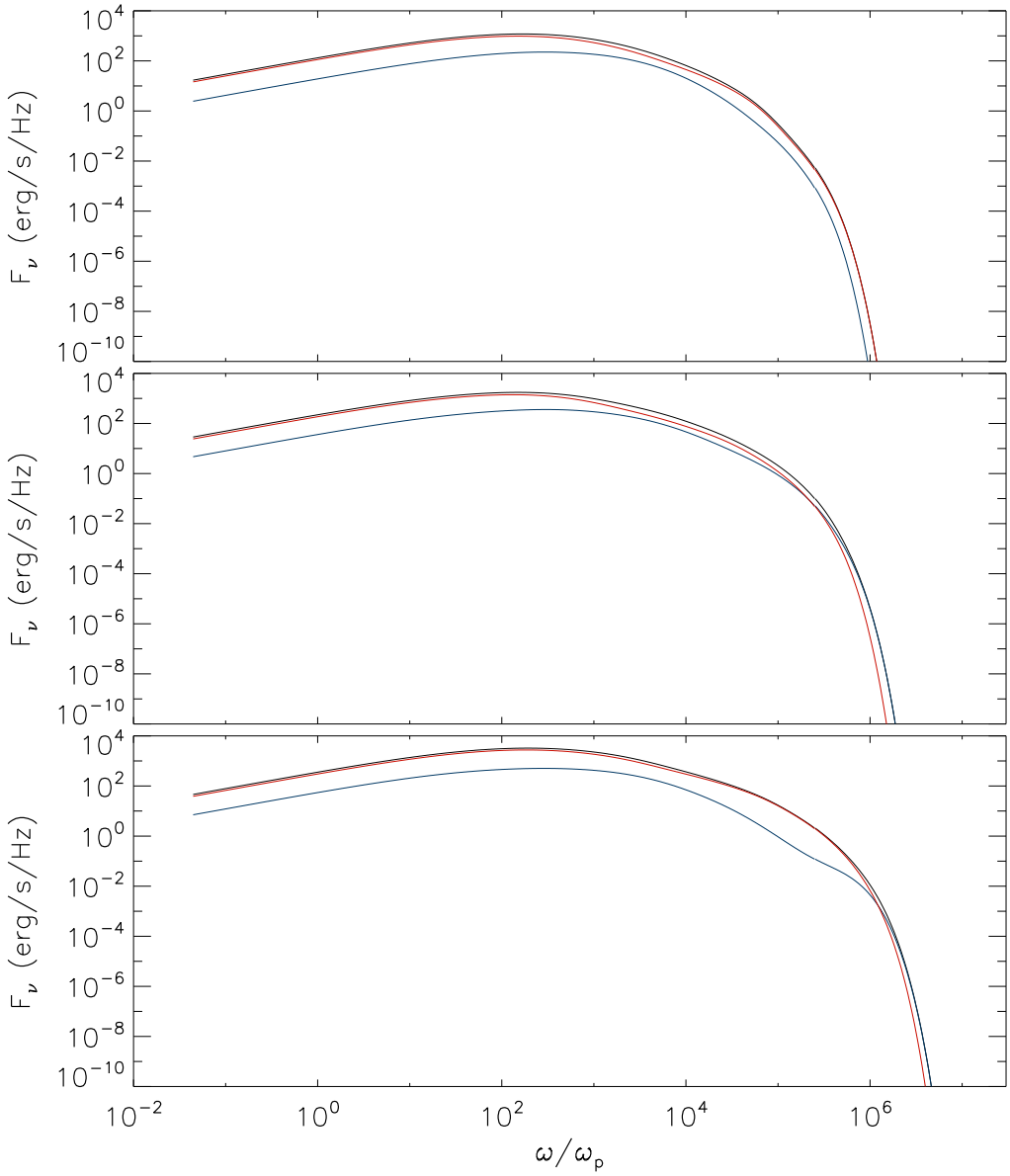

Figure 5.4: Radiation spectrum produced by a shock at a density ratio 100:1, at $\omega_p t =$ 900 (top), 1574 (middle), and 2250 (bottom). Red lines: Reverse shock spectrum. Blue lines: Forward shock spectrum. Black lines: Combined spectrum.

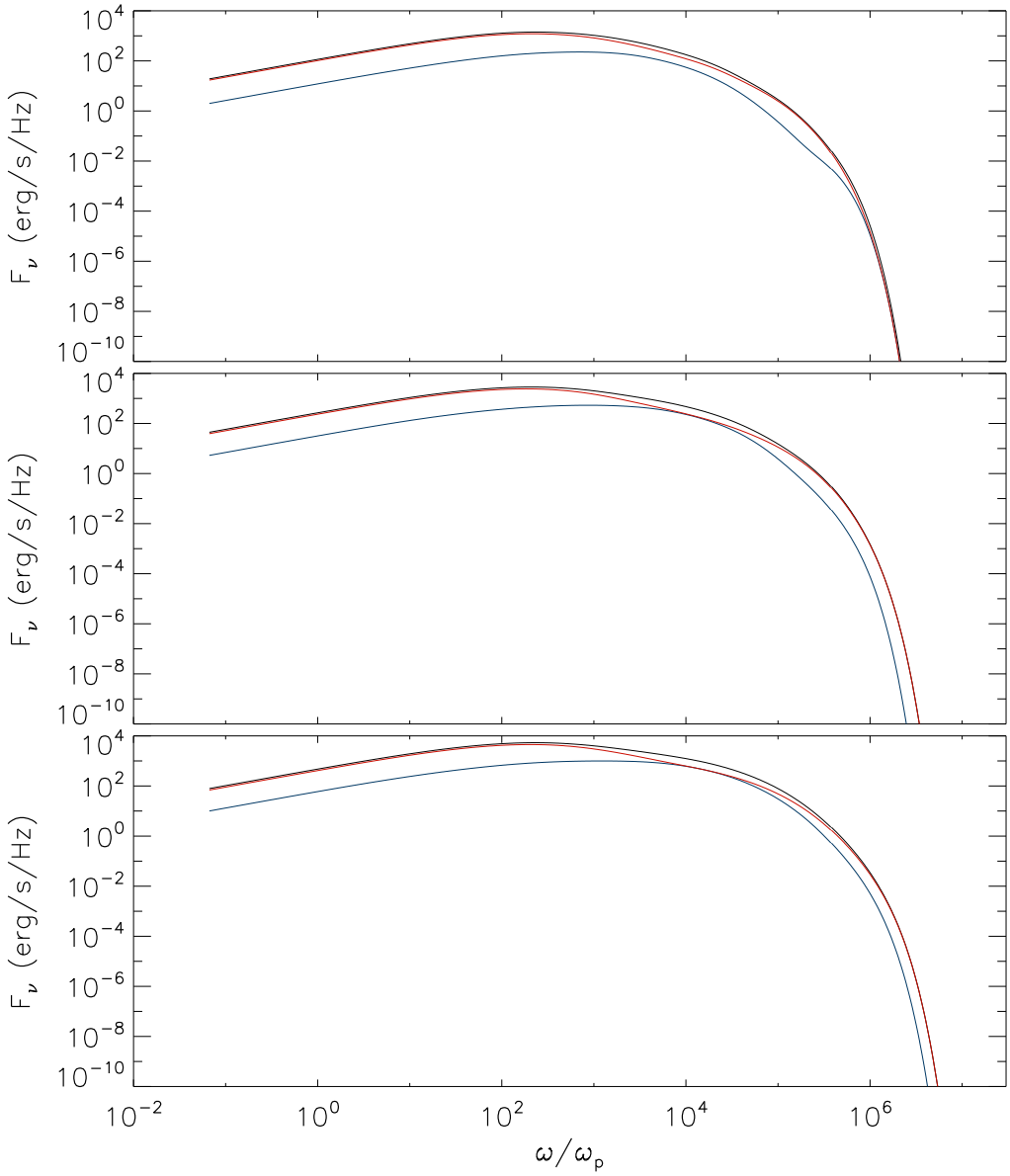

Figure 5.5: Radiation spectrum produced by a shock at a density ratio 200:1, at $\omega_p t =$ 540 (top), 1215 (middle), and 1890 (bottom). Red lines: Reverse shock spectrum. Blue lines: Forward shock spectrum. Black lines: Combined spectrum.

Chapter 6

Discussion and Conclusions

The shock simulations discussed in Chapter 4 showed the evolution in time of several properties of shocks formed by the interaction between a jet and an ambient medium, as is the case in the external shocks between a GRB jet and the ISM. Many of these properties, such as the magnetic fields generated, particle acceleration at the forward and reverse shocks, and mixing between the two plasmas would have an effect on the emission generated by the propagation of the shock through the ISM, and may be responsible for some of the observed properties of GRBs.

We found that at low density contrasts between the GRB jet and ISM material, the compression ratios in the shocked regions conformed well to our analytical expectations in the case of an ultrarelativistic reverse shock. Additionally, a significant amount of jet material was able to penetrate the ISM material built up behind the forward shock and and reach the region ahead of the forward shock. As the density contrast grows between the two regions, the analytical expectations for the compression ratios fit the simulations less well because the reverse shock is slowing down. Further, the mixing between the two plasmas shifts direction and the ISM material begins to penetrate the reverse shock.

The magnetic fields generated at the forward and reverse shocks also depend on

the density contrast between the two plasmas. As the jet material becomes denser, the forward shock is pushed faster and generates a stronger magnetic field. Although the magnetic field at the forward shock reaches a greater magnitude at its peak, the magnetic field at the reverse shock is generally wider and the region of possible particle accleration covers a larger region. At high density contrasts, it is also clear that the reverse shock accelerates particles by Fermi acceleration much more efficiently than does the forward shock.

The properties of these simulated shocks allowed us to predict the radiation spectra that would be produced by synchrotron emission in Chapter 5. We found that shocks at higher density contrasts produced spectra with a peak F_ν that was both much more luminous and located at higher frequency than the peak of the spectra produced at low density contrast between the two plasmas. For all density ratios simulated, the radiation spectrum generated was dominated by emission produced at the reverse shock by accelerated particles.

Appendix A

Relativistic Elastic Collisions

Alexander Tchekhovskoy

Two masses, M and m, collide with each other elastically, with initial velocities, V and v, parallel to each other. In the limit of $M \ggg m$, what is the final velocity, v', of the smaller mass, m?

A.1 Introduction

In the following two sections we will consider collisions in 1D (§A.2) and 2D (§A.3).

A.2 1D consideration

Let a massive body, moving with mass M, velocity $\vec{V} = V\hat{e}_x$, and Lorentz factor Γ, collide elastically with an object of mass m, velocity $\vec{v} = v\hat{e}_x$, and Lorentz factor,

$$\gamma = (1 - v^2)^{-1/2}. \tag{A.1}$$

Let us take the metric $\mathrm{diag}(1, -1, -1, -1)$.

The conservation of 4-momentum is:

$$\underline{P} + \underline{p} = \underline{P}' + \underline{p}', \tag{A.2}$$

where primes indicate quantities after the collision. Let us rearrange the terms and take the equation to 2nd power:

$$[(\underline{P} + \underline{p}) - \underline{p}']^2 = (\underline{P}')^2, \tag{A.3}$$

or

$$(\underline{P} + \underline{p})^2 - 2(\underline{P} + \underline{p})\underline{p}' + m^2 = M^2. \tag{A.4}$$

Grouping all known terms on the left-hand side and the unknown terms on the right-hand side, we obtain:

$$(\underline{P} + \underline{p})^2 + m^2 - M^2 = 2(\underline{P} + \underline{p})\underline{p}'. \tag{A.5}$$

Expanding in terms of components, we get:

$$\begin{aligned} &M^2 + 2(M\Gamma m\gamma - M\Gamma V m\gamma v) + m^2 + m^2 - M^2 \\ &\quad = 2\left[(M\Gamma + m\gamma)m\gamma' - (M\Gamma V + m\gamma v)m\gamma' v'\right] \end{aligned} \tag{A.6}$$

Assuming $M/m \gg \gamma/\Gamma$, collecting the terms, and dividing by $2mM\Gamma$, we obtain:

$$\gamma(1 - Vv) + \frac{m}{M\Gamma} = \gamma'(1 - Vv') \tag{A.7}$$

We can proceed further by dropping the second term on the left-hand side, which requires $M\Gamma\gamma(1 - Vv) \gg m$, or equivalently, *both* $\gamma M \gg \Gamma m$ and $\Gamma M \gg \gamma m$:

$$\gamma(1 - Vv) = \gamma'(1 - Vv'), \quad M/m \gg \{\gamma/\Gamma, \Gamma/\gamma\}. \tag{A.8}$$

Resolving (A.8) for v', the velocity of mass m after the collision, we obtain:

$$v' = \frac{2V - v(1+V^2)}{1+V^2-2vV}, \quad M/m \gg \{\gamma/\Gamma, \Gamma/\gamma\}. \tag{A.9}$$

Note that our assumptions do not rule out $\gamma \gg \Gamma$. We note also that in the limit $v \to 0$, formula (A.9) reduces to the well-known result for relativistic addition of velocities:

$$v' \overset{v\to 0}{=} \frac{V+V}{1+VV/c^2}, \tag{A.10}$$

where I restored the factors of the speed of light for clarity. Using eq. (A.9), we can easily obtain the 4-velocity of mass m after the collision:

$$u' = \Gamma^2\gamma\left[2V - v(1+V^2)\right] \overset{v\ll 1}{=} 2\Gamma^2 V\gamma, \quad M/m \gg \{\gamma/\Gamma, \Gamma/\gamma\}, \tag{A.11}$$

where the last approximate equality is as people anticipated.

A.3 2D consideration

Now consider mass m moving at an angle to the wall. We set the spatial components of 4-velocity as follows:

$$\vec{u} = u_x\hat{e}_x + u_y\hat{e}_y = \gamma(v_x\hat{e}_x + v_y\hat{e}_y), \tag{A.12}$$

where by definition,

$$\gamma = (1 + u_x^2 + u_y^2)^{1/2} = (1 - v_x^2 - v_y^2)^{-1/2}. \tag{A.13}$$

Let us derive (A.8) directly for a collision of a wall with an infinite mass, $M = \infty$, and with 4-velocity $\vec{U} = U_x\hat{e}_x = V\hat{e}_x$, with a body of mass m moving with a 4-velocity

$\vec{u}$ given by (A.12). Since the wall has an infinite mass, its velocity is conserved during the collision: $\underline{U} = \underline{U}'$. In the frame of the wall, the normal component of the body changes sign and the parallel component stays constant. Therefore, the relative Lorentz factor of the body with respect to the wall the wall is also conserved during the collision:

$$\gamma_{\rm rel} \equiv \underline{U} \cdot \underline{u} = \underline{U}' \cdot \underline{u}'. \tag{A.14}$$

In components, this equation becomes

$$\gamma_{\rm rel} \equiv \Gamma(\gamma - V u_x) = \Gamma(\gamma' - V u'_x), \tag{A.15}$$

where $\underline{u} = (\gamma, u_x, u_y) = \gamma(1, v_x, v_y)$, $\underline{U}' = \underline{U} = \Gamma(1, V, 0)$. Cleaning up,

$$\gamma - V u_x = \gamma' - V u'_x, \tag{A.16}$$

which is equivalent to (A.8).

In the lab frame, only the $x-$component of momentum, $p_x \equiv m u_x$, changes during the collision. The $y-$component of momentum, $p_y \equiv m u_y$, is directed parallel to the wall, and is conserved during the collision. Therefore, during the collision the $y-$component of 4-velocity remains constant:

$$u'_y = u_y. \tag{A.17}$$

Combining equations (A.13), (A.16), and (A.17), we obtain:

$$\gamma - V u_x = \sqrt{1 + {u'_x}^2 + u_y^2} - V u'_x. \tag{A.18}$$

This results in a quadratic equation for the only unknown, u'_x. The two roots of the quadratic are given by (one can analytically take the root of the discriminant, and it

is for a good reason):

$$u'_x = \Gamma^2 \left[V(\gamma - u_x V) \pm (u_x - \gamma V) \right]. \tag{A.19}$$

One of the roots is trivial: $u'_x = u_x$. This one corresponds to no collision. We are interested in the other root:

$$u'_x = \Gamma^2 \gamma \left[2V - v_x(1 + V^2) \right]. \tag{A.20}$$

Surprisingly, the answer is symbolically identical to the 1-D treatment, eq. (A.11), however, as opposed to (A.11), here the definition of γ is includes v_y (compare eq. (A.13) to (A.1)). For given pre-collision components of 4-velocity, u_x and u_y, of the body, post-collision 4-velocity components, u'_x and u'_y, are given by (A.20) and (A.17).

Bibliography

Bloom, J. S. 2011, What Are Gamma-Ray Bursts?, ed. Bloom, J. S.

Buneman, O. 1993, in Computer Space Plasma Physics, Simulation Techniques and Software, ed. H. Matsumoto & Y. Omura (Tokyo: Terra Scientific Publishing Company), 67–84

Johnson, M. H. & McKee, C. F. 1971, Physical Review D, 3, 858

Piran, T. 2004, Reviews of Modern Physics, 76, 1143

Rosswog, S. & Bruggen, M. 2003, Introduction to High-Energy Astrophysics, ed. Rosswog, S. & Bruggen, M.

Sari, R. & Piran, T. 1995, ApJL, 455, L143+

Spitkovsky, A. 2005, in American Institute of Physics Conference Series, Vol. 801, Astrophysical Sources of High Energy Particles and Radiation, ed. T. Bulik, B. Rudak, & G. Madejski, 345–350

Spitkovsky, A. 2008, ApJL, 682, L5